

# Global Biogeochemical Cycles

## RESEARCH ARTICLE

10.1029/2020GB006863

### Key Points:

- The mean number of passages through the biological pump per carbon molecule is a natural metric of pump efficiency
- Globally averaged  $44 \pm 4\%$  of the dissolved carbon in a given water parcel is biologically pumped with  $0.65 \pm 0.08$  lifetime passages per molecule
- Changes in atmospheric  $\text{CO}_2$  are related to changes in the mean number of pump passages and the mean injection-tagged sequestration time

### Correspondence to:

M. Holzer,  
[mholzer@unsw.edu.au](mailto:mholzer@unsw.edu.au)

### Citation:

Holzer, M., Kwon, E. Y., & Pasquier, B. (2021). A new metric of the biological carbon pump: Number of pump passages and its control on atmospheric  $\text{pCO}_2$ . *Global Biogeochemical Cycles*, 35, e2020GB006863. <https://doi.org/10.1029/2020GB006863>

Received 16 OCT 2020

Accepted 3 MAY 2021

## A New Metric of the Biological Carbon Pump: Number of Pump Passages and Its Control on Atmospheric $\text{pCO}_2$

Mark Holzer<sup>1</sup> , Eun Young Kwon<sup>2,3</sup> , and Benoit Pasquier<sup>4</sup> 

<sup>1</sup>Department of Applied Mathematics, School of Mathematics and Statistics, University of New South Wales, Sydney, NSW, Australia, <sup>2</sup>Center for Climate Physics, Institute for Basic Science, Busan, South Korea, <sup>3</sup>Pusan National University, Busan, South Korea, <sup>4</sup>Department of Earth Sciences, University of Southern California, Los Angeles, CA, USA

**Abstract** We develop novel locally defined diagnostics for the efficiency of the ocean's biological pump by tracing carbon throughout its lifetime in the ocean from gas injection to outgassing and counting the number of passages through the soft-tissue and carbonate pumps. These diagnostics reveal that the biological pump's key controls on atmospheric  $\text{pCO}_2$  are the mean number of lifetime pump passages per dissolved inorganic carbon (DIC) molecule at the surface and the mean aphotic sequestration time of regenerated DIC. We apply our diagnostics to an observationally constrained carbon-cycle model that features spatially varying stoichiometric ratios and is embedded in a data-assimilated global ocean circulation. We find that for the present-day ocean an average of  $44 \pm 4\%$  of DIC in a given water parcel makes at least one lifetime passage through the soft tissue pump, and about 4% makes at least one passage through the carbonate pump. The global mean number of lifetime pump passages per molecule, including the fraction with zero passages, is  $\bar{N}_{\text{soft}} = 0.65 \pm 0.08$  and  $\bar{N}_{\text{carb}} \sim 0.04$  for the soft-tissue and carbonate pumps. Using idealized perturbations to sweep out a sequence of states ranging from zero biological activity ( $\text{pCO}_2^{\text{atm}} = 493 \pm 1$  ppmv) to complete surface nutrient depletion ( $\text{pCO}_2^{\text{atm}} = 207 \pm 1$  ppmv), we find that fractional changes in  $\text{pCO}_2^{\text{atm}}$  are dominated by fractional changes in the number of soft-tissue pump passages. At complete surface nutrient depletion, the mean fraction of DIC that has at least one lifetime passage through the soft-tissue pump increases to  $69 \pm 5\%$  with  $\bar{N}_{\text{soft}} = 1.6 \pm 0.3$ .

**Plain Language Summary** Tiny plants floating near the ocean surface use sunlight to convert nutrients and dissolved  $\text{CO}_2$  into organic matter. A fraction of this organic matter sinks, transferring carbon from the surface to the deep ocean, a process known as the biological pump. The biological pump reduces atmospheric  $\text{CO}_2$  and is thus important for moderating climate. The organic matter is oxidized by microbes, which regenerates inorganic carbon that can then pass through the biological pump again or return to the atmosphere. Here, we calculate, for the first time, the number of passages through the biological pump that a typical carbon molecule makes during its lifetime in the ocean. This carbon-based measure of pump efficiency is useful for quantifying the biological pump's control on atmospheric  $\text{CO}_2$ . We find that in the current state of the ocean  $44 \pm 4\%$  of the dissolved inorganic carbon makes at least one lifetime passage through the biological pump, with a mean number of  $0.65 \pm 0.08$  passages per molecule. In numerical experiments that stimulate the biological pump to utilize all available nutrients, the fraction with at least one passage increases to  $69 \pm 5\%$  with  $1.6 \pm 0.3$  passages per molecule, which draws down atmospheric  $\text{CO}_2$  by about 70 ppmv.

## 1. Introduction

The ocean's biological pump consists of the uptake of inorganic carbon and nutrients by phytoplankton in the sunlit upper ocean followed by the export of a fraction of the biologically fixed carbon to depth (e.g., Ducklow et al., 2001). Because of their very different dynamics, it is useful to distinguish the soft-tissue pump driven by sinking organic particles and subducted dissolved organic matter, and the carbonate pump driven by sinking biogenic calcium carbonate ( $\text{CaCO}_3$ ) (e.g., Volk & Hoffert, 1985). The organic matter is oxidized in the ocean interior through microbial respiration and  $\text{CaCO}_3$  particles dissolve in undersaturated water at depth, both processes regenerating dissolved inorganic carbon (DIC) that is then available to cycle through the pump again. By sequestering carbon in the ocean interior, the biological pump is a key control on atmospheric  $\text{CO}_2$  and hence climate (e.g., Archer et al., 2000; Bacastow & Maier-Reimer, 1990;

McKinley et al., 2017; Sarmiento & Toggweiler, 1984). The biological pump's ability to sequester carbon is determined by the subtle interplay between biogenic particle transport and ocean circulation (DeVries et al., 2012; Kwon et al., 2009; Primeau et al., 2013; Pasquier & Holzer, 2016).

Past changes in the partial pressure of atmospheric CO<sub>2</sub> (pCO<sub>2</sub><sup>atm</sup>) and climate have been linked to changes in biological pump efficiency caused by both changes in physical circulation (e.g., changes in Southern Ocean ventilation driven by changes in winds and ice cover) and changes in biological productivity (e.g., driven by changes in dissolved iron availability) (for an overview, see Hain et al., 2014). To understand the role of the biological pump in the climate system it is therefore useful to be able to quantify the strength and efficiency of the biological pump and to relate these to pCO<sub>2</sub><sup>atm</sup>. Pump strength is commonly quantified in terms of new production (Dugdale & Goering, 1967; Eppley & Peterson, 1979; Gnanadesikan et al., 2002) or the closely related export production, which can be defined as the rate with which organic matter exported from the euphotic zone is respired in the aphotic zone (e.g., Primeau et al., 2013). Pump efficiency, sometimes also referred to as export efficiency, has been quantified in terms of the vertical gradients of DIC (e.g., Buesseler et al., 2020; Volk & Hoffert, 1985) and in terms of the fraction of the phosphate inventory that is regenerated (DeVries et al., 2012; Ito & Follows, 2005; Pasquier & Holzer, 2016; Sigman & Boyle, 2000). A nutrient-based metric of pump efficiency is attractive because nutrients limit export production, and the complete utilization of nutrients in the surface ocean represents a natural asymptote of the biological pump. However, relating regenerated phosphate inventories to regenerated carbon inventories has relied on knowledge of the C:P stoichiometric ratio, which has been shown to have substantial regional variations (Galbraith & Martiny, 2015; Teng et al., 2014) that decouple the nutrient and carbon cycles to some degree. A natural extension of the phosphate-based pump efficiency is to consider the inventory of regenerated DIC directly, which is also bounded by complete nutrient utilization. However, unlike for phosphate the maximum possible regenerated carbon inventory is not known from the outset, and only about 6% of the DIC is regenerated in the current state of the ocean even though the soft-tissue pump is thought to control about 60% of the variations in pCO<sub>2</sub><sup>atm</sup> across a wide range of possible climates (Cameron et al., 2005).

Here, we consider the number of pump passages that the carbon in DIC undergoes during its lifetime in the ocean, from injection by the atmosphere to exit from the ocean, as a natural metric for the efficiency of the biological pump. The mean number of pump passages and the closely related fraction of DIC undergoing at least one lifetime pump passage are defined locally. Aside from its conceptual appeal, the mean number of pump passages following carbon injection from the atmosphere has a natural connection with the resulting DIC regeneration rate. This regeneration rate can in turn be linked to the regenerated DIC inventory through an appropriately defined sequestration time which quantifies the time that the regenerated DIC stays below the euphotic zone. In this way, we link changes in the mean number of lifetime passages through the soft-tissue and carbonate pumps with changes in pCO<sub>2</sub><sup>atm</sup>. To illustrate and explore the number of carbon passages through the biological pump as a metric of pump efficiency, we use a relatively simple data-constrained model of the global carbon and phosphorus cycles embedded in a data-assimilated global circulation. For the current state of the ocean, we find that on average 40%–47% of the DIC in a given water parcel has at least one carbon pump passage during its lifetime. By considering highly idealized perturbations to vary the pump strength from zero to complete nutrient utilization, we show that, for a given circulation, the fractional change in the mean number of passages through the soft-tissue pump is the dominant control on atmospheric CO<sub>2</sub>.

## 2. Model and Numerical Experiments

### 2.1. Carbon Model

We embed relatively simple models of the ocean's phosphorus and carbon cycles with prescribed functional forms for the particle-flux profiles (Kwon & Primeau, 2008; Najjar et al., 1992) in a global steady ocean circulation using version two of the ocean circulation inverse model of DeVries (2014) (OCIM2, DeVries & Holzer, 2019). Key biogeochemical parameters are determined by minimizing the mismatch with observed DIC, phosphate (PO<sub>4</sub>), and total alkalinity (TA). For the phosphorus cycle, we carry three explicit tracers: PO<sub>4</sub>, particulate organic phosphorus (POP), and semi-labile dissolved organic phosphorus (DOP). The model equations for the phosphorus cycle are:

$$\begin{aligned}
 \mathcal{T}[\text{PO}_4] &= -U_p + \kappa_{\text{dop}}[\text{DOP}] - \gamma_g([\text{PO}_4] - \overline{[\text{PO}_4]}), \\
 \mathcal{T}[\text{DOP}] &= \sigma U_p - \kappa_{\text{dop}}[\text{DOP}] + k_{\text{pop}}[\text{POP}], \\
 \mathcal{T}_{\text{pop}}[\text{POP}] &= (1 - \sigma)U_p - k_{\text{pop}}[\text{POP}].
 \end{aligned} \tag{1}$$

Here,  $\mathcal{T}$  is the advective-diffusive flux-divergence operator,  $\mathcal{T}_{\text{pop}}$  is the flux-divergence operator for the sinking POP flux,  $U_p$  is the local phosphate uptake rate per unit volume,  $\kappa_{\text{dop}}^{-1}$  is the remineralization timescale, and  $k_{\text{pop}}^{-1}$  is the POP dissolution timescale. Both  $\kappa_{\text{dop}}$  and  $k_{\text{pop}}$  are modeled as globally uniform. (More details on  $U_p$  are provided below.) Because there are no external sources and sinks of phosphorus in our model, the total amount is specified by weakly restoring  $[\text{PO}_4]$  to the observed global mean  $\overline{[\text{PO}_4]}$  with timescale  $\gamma_g^{-1} = 10^6$  years. Without prescribing the total amount of phosphorus in this way there would be no unique solution to the steady-state Equations 1; in particular, if  $U_p$  is linear in phosphate the resulting linear system would be rendered rank-deficient by the mass-conservation property of the flux-divergence operators. (This contrasts with time-stepped models where, in the absence of external sources and sinks, the total amount of phosphorus is set by the initial conditions.)

We model four carbon pools in addition to TA: DIC, semi-labile dissolved organic carbon (DOC), particulate inorganic carbon (PIC, i.e., biogenic  $\text{CaCO}_3$ ), and particulate organic carbon (POC). The concentrations obey

$$\begin{aligned}
 \mathcal{T}[\text{DIC}] &= -U_c - R(1 - \sigma)U_c + \kappa_{\text{doc}}[\text{DOC}] + k_{\text{pic}}[\text{PIC}] + S, \\
 \mathcal{T}[\text{DOC}] &= \sigma U_c - \kappa_{\text{doc}}[\text{DOC}] + k_{\text{poc}}[\text{POC}], \\
 \mathcal{T}_{\text{pic}}[\text{PIC}] &= R(1 - \sigma)U_c - k_{\text{pic}}[\text{PIC}], \\
 \mathcal{T}_{\text{poc}}[\text{POC}] &= (1 - \sigma)U_c - k_{\text{poc}}[\text{POC}].
 \end{aligned} \tag{2}$$

Here,  $U_c$  is the local DIC uptake rate per unit volume (biological production rate),  $\sigma$  is the fraction of production that immediately results in DOC without passing through the particulate pool first, and  $\kappa_{\text{doc}}^{-1}$  is the respiration timescale.  $\mathcal{T}_{\text{poc}}$  and  $\mathcal{T}_{\text{pic}}$  are the flux-divergence operators of the sinking particles and  $R$  is the corresponding PIC/POC rain ratio, approximated here as globally uniform. The coefficients  $k_{\text{poc}}^{-1}$  and  $k_{\text{pic}}^{-1}$  are the timescales for particle dissolution.

Particles are not advected with the flow here, but fall through the water column with a prescribed vertical velocity profile. Organic particles ([POP] and [POC]) fall with a mean speed that increases linearly with depth yielding a Martin curve characterized by exponent  $b$ , while carbonate particles (PIC) are modeled as falling at constant speed leading to an exponential flux-divergence profile characterized by the PIC remineralization length scale  $L_{\text{PIC}}$  (approximating the PIC flux-divergence profile by an exponential was first suggested by Yamanaka and Tajika [1996]). For simplicity, we assume the same profile for POC and POP so that  $\mathcal{T}_{\text{poc}} = \mathcal{T}_{\text{pop}}$ . Explicit particle tracers are used here primarily for conceptual and coding convenience; we assume rapid particle dissolution (routinely modeled as instant, e.g., Najjar et al., 1992) and set  $k_{\text{pop}} = k_{\text{poc}} = k_{\text{pic}} = 1/\text{day}$ . While the inverse timescales  $\kappa_{\text{doc}}$  (DOC respiration) and  $\kappa_{\text{dop}}$  (DOP remineralization) are optimized, for simplicity we take  $\kappa_{\text{doc}} = \kappa_{\text{dop}}$ . The parameters  $\sigma$ ,  $\kappa_{\text{doc}}$ ,  $b$ ,  $L_{\text{PIC}}$ , and  $R$ , are all approximated as globally uniform.

The term  $S$  in the DIC equation of 2 represents the source/sink of [DIC] due to air-sea exchange given by  $S = (1 / \Delta z_1)K_w K_0 (\text{pCO}_2^{\text{atm}} - \text{pCO}_2^{\text{ocn}})$ , where  $\Delta z_1$  is the thickness of the model's surface layer,  $K_0$  is the temperature and salinity-dependent  $\text{CO}_2$  solubility computed from the parametric fits of Weiss (1974), and  $\text{pCO}_2^{\text{atm}}$  is the partial pressure of  $\text{CO}_2$  in the atmosphere. The seawater  $\text{pCO}_2^{\text{ocn}}$  equivalent partial pressure of dissolved  $\text{CO}_2$  is computed by solving the nonlinear seawater carbon chemistry using the CO2SYS code (van Heuven et al., 2011). For parameter optimization, we prescribe  $\text{pCO}_2^{\text{atm}} = 278$  ppmv. When perturbing the optimized system as described further below,  $\text{pCO}_2^{\text{atm}}$  is determined by carbon conservation, with the approximation that the total amount of carbon in the atmosphere-ocean system is constant. We solve this conservation constraint jointly with Equation 2. The piston velocity is parameterized as  $K_w = s_w a (1 - f_{\text{ice}})U^2(\text{Sc}/660)^{-1/2}$ , where  $U^2$  is the climatological squared surface wind speed,  $f_{\text{ice}}$  is the climatological sea-ice fraction, and  $a = 0.251 \text{ cm h}^{-1} \text{ m}^{-2} \text{ s}^2$  (Wanninkhof et al., 2013) and  $s_w$  is a fine-tuning scale factor

that was jointly optimized to  $s_w = 1.2$ .  $U^2$  and  $f_{ice}$  were calculated as averages of 6-h NCEP reanalysis for the period 1948–2014 (Kalnay et al., 1996). The temperature-dependent  $\text{CO}_2$  Schmidt number  $Sc$  was calculated using the empirical fits of Wanninkhof (1992).

The biological phosphate uptake  $U_p$  is parameterized in terms of the modeled phosphate concentration as  $U_p = \mathcal{L}[\text{PO}_4]$ , where the field of uptake coefficients  $\mathcal{L}$  (inverse timescales) is parameterized in terms of satellite-data-derived net primary production per unit area (NPP). The idea is that  $U_c \propto (\text{NPP})^\beta$  for some positive power  $\beta$  (Hansell et al., 2012; Teng et al., 2014), and  $U_p = R_{p:c} U_c$ , where  $R_{p:c}$  is the stoichiometric P:C uptake ratio. We thus have for points  $\mathbf{r} = (x, y, z_i)$  in the  $i$ th model layer of the euphotic zone (approximated as the top 73 m, spanning the top two layers)

$$\mathcal{L}(\mathbf{r}) = R_{p:c}(\mathbf{r}) \alpha \left( \frac{\text{NPP}(x, y)}{J_0 \Delta z_i} \right)^\beta \frac{1}{[\text{PO}_4]_{\text{obs}}(\mathbf{r})}, \quad (3)$$

where  $\Delta z_i$  is the thickness of the  $i$ th layer,  $J_0 \equiv 1 \text{ mg C/m}^3/\text{day}$  nondimensional NPP/ $\Delta z_i$ ,  $\alpha$  and  $\beta$  are globally uniform constants determined through optimization, and  $[\text{PO}_4]_{\text{obs}}$  is the observed phosphate concentration. We parameterize the P:C uptake ratio of the soft-tissue pump in terms of the observed phosphate concentration following Galbraith and Martiny (2015):

$$R_{p:c} = m_{p:c} [\text{PO}_4]_{\text{obs}} + b_{p:c}. \quad (4)$$

The biological  $\text{PO}_4$  and DIC uptake fields are then given in terms of  $\mathcal{L}$  and the modeled  $[\text{PO}_4]$  as

$$U_p = \mathcal{L}[\text{PO}_4] \quad \text{and} \quad U_c = R_{c:p} U_p. \quad (5)$$

TA is governed by (e.g., Murnane et al., 1999)

$$T[\text{TA}] = 2J_{\text{bCaCO}_3} - R_{N:P} J_{\text{bPO}_4} - \gamma_g([\text{TA}] - \overline{[\text{TA}]}), \quad (6)$$

where  $J_{\text{bCaCO}_3} \equiv k_{\text{pic}}[\text{PIC}] - R(1 - \sigma)U_c$  and  $J_{\text{bPO}_4} \equiv k_{\text{dop}}[\text{DOP}] - U_p$  are the source-minus-sink terms for  $\text{CaCO}_3$  and  $\text{PO}_4$ , respectively, and  $R_{N:P} = 16 + 1 + 2 \times 2.4$  is an augmented stoichiometric ratio to account not only for the contributions to TA from  $\text{NO}_3^-$  (16:1), but also from  $\text{PO}_4^{3-}$  itself and from  $\text{SO}_4^{2-}$  and  $\text{HSO}_4^-$  (see Wolf-Gladrow et al., 2007). We have zero net sources or sinks of TA and hence specify the observed global mean  $\overline{[\text{TA}]}$  through weak relaxation similar to what is done for phosphate.

We additionally included virtual source/sink terms for DIC and TA to account for the concentration/dilution effects of evaporation/precipitation (Murnane et al., 1999), but have omitted these terms from the equations here for clarity of presentation. Anthropogenic DIC,  $C_{\text{ant}}$ , is estimated by propagating the atmospheric time history from pre-industrial time to the year 2002, the nominal year of the DIC observations used (see next section).  $C_{\text{ant}}$  is added to the DIC from the solutions of the carbon model (2) before calculating the mismatch with observations. (For the purpose of calculating the mismatch with observations, TA and  $\text{PO}_4$  are approximated as unchanged from preindustrial times.)

## 2.2. Observational Data and Parameter Optimization

The values of key biogeochemical model parameters are obtained by minimizing the volume-weighted quadratic mismatch of DIC,  $\text{PO}_4$ , and TA with the observed gridded annual-mean fields. The gridded observed fields for  $\text{PO}_4$  and silicic acid (the latter is used only for alkalinity in the carbon chemistry solver) were taken from the World Ocean Atlas (Garcia et al., 2010), and the gridded DIC and TA fields, nominally for the year 2002, are from the Global Data Analysis Project Version 2 (GLODAP2, Olsen et al., 2016). The time history of  $\text{pCO}_2^{\text{atm}}$  needed to estimate the  $C_{\text{ant}}$  distribution was taken from the Goddard Institute for Space Studies (GISS) data set for the period 1850 to present and extended back to 1720 using ice-core data (Etheridge et al., 1998). This GISS data set was constructed from the following observations: data for the period before 1958 is from measurements of Antarctic ice cores (Etheridge et al., 1996), data for 1958–1974 is from the Scripps Institution of Oceanography air-sampling network (Keeling et al., 2005), and data from 1975 onward is from

flask measurements by the National Oceanic and Atmospheric Administration (NOAA) Global Monitoring Laboratory (GML) Carbon Cycle Cooperative Global Air Sampling Network (Dlugokencky et al., 2021) and from in situ measurements at the NOAA Baseline Observatories (Thoning et al., 2021).

We explored two types of satellite-derived NPP estimates available from Oregon State University: VGPM calculated from the Vertically Generalized Production Model (Behrenfeld & Falkowski, 1997), and CbPM from the Carbon-based Production Model-2 (Westberry et al., 2008). The optimized parameters for either NPP type are very similar, with the small spread between VGPM and CbPM indicating parameter uncertainty due to uncertainty in NPP. The resulting optimized respiration timescale  $\kappa_{\text{dop}}^{-1}$  had a value of 2.5 years, which is about twice as long as that estimated by Teng et al. (2014). We therefore also considered two optimizations (for VGPM and CbPM NPP) with  $\kappa_{\text{dop}}^{-1}$  held fixed at 1.2 years to quantify the sensitivity to this uncertain parameter, which is key for counting pump passages. We find that the spread between the optimized VGPM and CbPM cases is again small, but that there are substantial adjustments in the parameters associated with biological production ( $\alpha$ ,  $\beta$ ,  $\sigma$ ). The overall fit with the 1.2-year respiration timescale is only slightly worse (0.5% larger overall quadratic misfit), with slightly larger root-mean-square (RMS) errors for DIC and  $\text{PO}_4$  but a slightly smaller RMS error for TA. The volume-weighted quadratic mismatch of each field ( $[\text{PO}_4]$ ,  $[\text{DIC}]$ , and  $[\text{TA}]$ ) is weighted by its global spatial variance, and the three weighted fields contribute equally to the cost function. The optimized states are characterized by a volume-weighted RMS mismatch of 0.15  $\mu\text{M}$  for  $\text{PO}_4$ , 19  $\mu\text{M}$  for DIC, and 14  $\mu\text{M}$  for TA. Appendix A specifies the precise cost function, lists the optimized parameter values, and the RMS errors for each case.

When presenting results below, we will show the VGPM case with optimized  $\kappa_{\text{doc}}$  as it has the best overall fit. When plotting global mean metrics for a sequence of perturbed states, we additionally show the values across all four cases (VGPM and CbPM with  $\kappa_{\text{doc}}^{-1} = 2.5$  and 1.2 years) for the base state and for two selected perturbations. The uncertainty in a given numerical value reported in the main text is the half-range across all four cases, which is dominated by differences in  $\kappa_{\text{doc}}$  (see also Appendix A).

### 2.3. Idealized Perturbations

To illustrate the behavior of our counting-based metrics for different states of the biological pump, we consider highly idealized perturbations that simply scale the uptake-rate coefficients (inverse timescales)  $\mathcal{L}$  up or down uniformly over the global ocean. For convenience, we quantify the strength of a given perturbation in terms of  $P^*$ , the ratio of the global regenerated  $\text{PO}_4$  inventory to the total  $\text{PO}_4$  inventory. In the limit as  $\mathcal{L} \rightarrow 0$  the biological pump shuts off, with  $P^*$  and all metrics of pump efficiency approaching zero. In the limit as  $\mathcal{L} \rightarrow \infty$ , all available nutrients are utilized so that  $P^* \rightarrow 1$  and our carbon pump metrics are expected to approach their maximum values. To achieve the  $P^* \rightarrow 1$  limit, it is necessary that all surface ocean points have non-zero production. We therefore filled-in the data voids of the satellite-derived NPP field over ice-covered regions in the Arctic and Weddell Seas with the seasonal minimum of NPP at the same latitude. Without such fill-in,  $P^*$  only reaches around 95% even as  $\mathcal{L} \rightarrow \infty$  because the patches of zero uptake remain a small source of preformed nutrients.

The effect of scaling up  $\mathcal{L}$  is to strengthen high-latitude nutrient trapping and biological production. The effect of scaling down  $\mathcal{L}$  is to decrease overall production and contract it into the subtropical gyres. This occurs because the spatial pattern of  $\mathcal{L}$  (which for simplicity is held fixed for these perturbations consistent with parameterization Equation 3 in terms of the observed NPP and  $\text{PO}_4$ ) is highest in the subtropical gyres and, as nutrient uptake is ever more diminished,  $\text{PO}_4$  becomes increasingly homogeneous so that the pattern of production is no longer dominated by nutrient availability but directly by the uptake-rate coefficients  $\mathcal{L}$ . (The spatial patterns of both the  $\text{PO}_4$  and DIC uptake-rate coefficients are held fixed because the variable C:P in Equation 4 is also keyed to the observed  $\text{PO}_4$  and hence invariant under these perturbations.) Whether or not this is a realistic scenario is at best debatable, but these perturbations do have the nice feature of smoothly enhancing the proportion of high-latitude nutrient utilization together with global mean production.

We consider quasi-continuous variations with  $P^*$  obtained by sweeping the perturbation factor,  $\lambda$ , by which the unperturbed  $\mathcal{L}$  is multiplied, from  $\lambda = 4.77 \times 10^{-5}$  to  $\lambda = 5.67 \times 10^4$  in multiplicative increments of 1.645, for a total of 42 nonlinear carbon systems, each of which is solved using Newton's method. The correspond-

ing values of  $P^*$  range from  $P^* = 1.7 \times 10^{-4}$  to  $P^* = 0.99978$ . We plot the values of global mean quantities for all perturbations to show their detailed  $P^*$  dependence. For demonstrating the effects of using different NPP products (VGPM and CbPM) or of using different respiration timescales, as well as for examining spatial patterns, we consider only a subset of 3 states for simplicity of presentation: the unperturbed state at  $P^* \simeq 0.44$ , the state with production throttled at  $P^* \simeq 0.037$  ( $\lambda = 0.011$ ), and the state with production “cranked up” at  $P^* \simeq 0.94$  ( $\lambda = 88$ ). For reference, the patterns of  $U_C$  for these three states and the pattern of  $\mathcal{L}$  are plotted in Appendix B.

### 3. Diagnostic Equations

#### 3.1. Linear Labeling Tracers

To trace carbon through the biological pump, we use linear labeling tracers organized into column vector  $\chi = [\chi_{\text{DIC}}; \chi_{\text{DOC}}; \chi_{\text{POC}}; \chi_{\text{PIC}}]$  (for other applications of labeling tracers, see Holzer et al., 2014; Pasquier & Holzer, 2016, 2018). We think of these labels as being attached to the carbon molecules and they therefore have the same concentrations, for example,  $\chi_{\text{DIC}} = [\text{DIC}]$ . The labeling tracers participate in all process (e.g., air-sea exchange, uptake, remineralization) in proportion to their concentration and thus obey equations linear in  $\chi$ . This allows us to partition  $\chi$  into component contributions such as the concentrations that pass through the biological pump a specific number of times. While most terms of Equation 2 are already linear in the carbon tracers, we need to replace the nonlinear carbon chemistry that controls air-sea exchange with an equivalent linear diagnostic operator for the labels. To that end, we split the DIC source/sink term  $S$  into atmosphere-to-ocean (AO) and ocean-to-atmosphere (OA) parts:

$$S = S_{\text{AO}} - \mathbf{s}_{\text{OA}} \chi. \quad (7)$$

$S_{\text{AO}}$  injects DIC labels into the ocean and is given by

$$S_{\text{AO}} \equiv \frac{K}{\Delta z_1} \text{pCO}_2^{\text{atm}}, \quad (8)$$

where  $K(\mathbf{r}) \equiv K_w(\mathbf{r})K_0(\mathbf{r})$ . Note that  $S_{\text{AO}}$  injects DIC labels but is independent of their concentrations. The OA sink of DIC labels is proportional to their concentration and thus cast in linear form as  $\mathbf{s}_{\text{OA}} \chi$ , where the diagonal operator  $\mathbf{s}_{\text{OA}}$  acts only on the  $\chi_{\text{DIC}}$  part of  $\chi$  at surface grid points  $\mathbf{r}_s$ . The entry of  $\mathbf{s}_{\text{OA}}$  for surface point  $\mathbf{r}_s$  is diagnosed from the solution of the nonlinear carbon-chemistry system as  $s_{\text{OA}}(\mathbf{r}_s) \equiv (K(\mathbf{r}_s) / \Delta z_1) \text{pCO}_2^{\text{ocn}}(\mathbf{r}_s) / [\text{DIC}](\mathbf{r}_s)$ . We also decouple the diagnostic equation for carbon labels from the phosphate cycle by defining a linear DIC uptake with the uptake-rate coefficients  $\mathcal{L}_C(\mathbf{r}) = U_C(\mathbf{r}) / [\text{DIC}](\mathbf{r})$  so that  $U_C$  is replaced by  $\mathbf{L}_C \chi_{\text{DIC}}$  in the linear diagnostic system, where  $\mathbf{L}_C = \text{diag}(\mathcal{L}_C)$ . The equations obeyed by the linear labeling tracers  $\chi$  are now obtained from Equation 2 by replacing  $[\text{DIC}]$  with  $\chi_{\text{DIC}}$ ,  $[\text{DOC}]$  with  $\chi_{\text{DOC}}$ ,  $[\text{PIC}]$  with  $\chi_{\text{PIC}}$ , and  $[\text{POC}]$  with  $\chi_{\text{POC}}$ , and replacing  $U_C$  and  $S$  with their linear labeling equivalents. Moving all linear terms of the discretized Equations 2 to the left-hand side and organizing them into a matrix  $\mathbf{A}$ , we can succinctly write the linear-equivalent system of diagnostic labeling tracers as

$$\mathbf{A} \chi = S_{\text{AO}}. \quad (9)$$

(Note that we displayed the terms of Equation 2 so that the structure of  $\mathbf{A}$  can easily be read off.) We emphasize that Equation 9 is not a linearization of the nonlinear carbon system, but instead describes the linear labeling tracers that are used to track carbon faithfully through the dissolved and particulate organic and inorganic carbon pools of the nonlinear system. By construction system 9 has exactly the same solutions as the nonlinear carbon system 2.

#### 3.2. Partitioning DIC According to the Number of Pump Passages

We define one passage through the biological pump as uptake followed by aphotic regeneration. We only consider aphotic regenerations here so that we can quantitatively link our pump diagnostic to the tradition-

al regenerated DIC inventory. Our treatment below is identical for the soft-tissue and carbonate pumps; we therefore use subscript  $p$  for the  $p$ -pump, with  $p$  either “soft” or “carb.” We partition the concentration of DIC at a given point into the fractions of DIC that have passed through the  $p$ -pump  $n$  times since injection from the atmosphere, and the fractions that will pass  $m$  times through the  $p$ -pump until exit from the ocean back into the atmosphere. (This is the only exit available in our model—we do not include any sediment burial.) Thus, for example, at every point  $\mathbf{r}$  in the ocean, we will calculate the concentrations  $\chi_p^n(\mathbf{r})$  that passed exactly  $n$  times through the  $p$ -pump in the past, which partitions the full concentration  $\chi(\mathbf{r})$  such that  $\sum_{n=0}^{\infty} \chi_p^n(\mathbf{r}) = \chi(\mathbf{r})$ .

The basic idea of counting the number of regenerations since injection from the atmosphere is to first remove the terms representing aphotic regeneration from Equation 9 to calculate the concentration of DIC that was never regenerated below the euphotic zone. We then let this concentration be regenerated once, transported, and taken up biologically without further regeneration to obtain the concentrations that passed exactly once through the pump. This process is repeated recursively to determine the concentrations that passed  $n$  times through the pump. To calculate the fraction of DIC making  $m$  passages in the future, we use the same idea but for the time-reversed adjoint. To proceed, we denote by  $\mathbf{R}_s$  and  $\mathbf{R}_c$  the soft-tissue and carbonate regeneration operators such that  $\mathbf{R}_s \chi = \kappa_{\text{doc}} \mathbf{M}_{\text{ap}} \chi_{\text{DOC}}$  is the respiration field in the aphotic zone ( $\mathbf{M}_{\text{ap}}$  is a diagonal operator that selects the aphotic zone) and  $\mathbf{R}_c \chi = k_{\text{pic}} \mathbf{M}_{\text{ap}} \chi_{\text{PIC}}$  is the aphotic PIC dissolution field. We denote the system operator without aphotic  $p$ -pump regeneration by  $\mathbf{B}_p \equiv \mathbf{A} + \mathbf{R}_p$  (plus because the regeneration appears as  $-\mathbf{R}_p$  in  $\mathbf{A}$ ).

Following Pasquier and Holzer (2018) it is straightforward to show the following: The concentration  $\chi_p^n$  that made  $n$  passages through the  $p$ -pump in the past since injection from the atmosphere is given recursively by

$$\chi_p^0 = \mathbf{B}_p^{-1} S_{\text{AO}}, \quad \text{with} \quad \chi_p^n = \mathbf{B}_p^{-1} \mathbf{R}_p \chi_p^{n-1} \quad \text{for} \quad n \geq 1. \quad (10)$$

Note that  $\chi(\mathbf{r}) = \sum_{n=0}^{\infty} \chi_p^n(\mathbf{r})$  so that the local fraction of  $\chi$  that passed  $n$  times through the  $p$ -pump is  $f_p^{n\downarrow} = \chi_p^n / \chi$ , with  $\sum_{n=0}^{\infty} f_p^{n\downarrow} = 1$ . (We use the  $\downarrow$  superscript on  $f$  to indicate that this is the fraction that passed through the pump since injection into ( $\downarrow$ ) the ocean.) The mean number of past passages  $\bar{n}_p = \sum_{n=0}^{\infty} n f_p^{n\downarrow}$  is efficiently computed from

$$\bar{n}_p = \mathbf{diag}^{-1}(\chi) \mathbf{A}^{-1} \mathbf{R}_p \chi, \quad (11)$$

which can be derived from Equations 9 and 10. Note that all four types of carbon (DIC, DOC, PIC, and POC) are partitioned by these equations—here we consider only fractions and mean number of passages defined by the DIC partitioning.

The local fraction  $f_p^{m\uparrow}$  that will make  $m$  passages through the  $p$ -pump in the future before escaping to the atmosphere is given by

$$f_p^{0\uparrow} = \tilde{\mathbf{B}}_p^{-1} \mathbf{s}_{\text{OA}} u, \quad \text{with} \quad f_p^{m\uparrow} = \tilde{\mathbf{B}}_p^{-1} \tilde{\mathbf{R}}_p f_p^{(m-1)\uparrow} \quad \text{for} \quad m \geq 1, \quad (12)$$

where  $u$  is a vector of unit elements, and  $\tilde{\mathbf{O}} \equiv \mathbf{W}^{-1} \mathbf{O}^T \mathbf{W}$  is the volume-weighted adjoint of any operator  $\mathbf{O}$ , with  $\mathbf{W} \equiv \mathbf{diag}([w, w, w, w])$ , for row vector  $w$  of grid-box volumes. (We use the  $\uparrow$  superscript on  $f$  to indicate that this is the fraction that will pass through the pump until exiting ( $\uparrow$ ) the ocean.) The corresponding mean number of future passages  $\bar{m}_p = \sum_{m=0}^{\infty} m f_p^{m\uparrow}$  is efficiently computed from

$$\bar{m}_p = \tilde{\mathbf{A}}^{-1} \tilde{\mathbf{R}}_p u, \quad (13)$$

which can be derived from Equation 12 and  $\tilde{\mathbf{A}} u = \mathbf{s}_{\text{OA}} u$ , expressing the fact that all carbon eventually returns to the atmosphere in the absence of other sinks (as modeled here).

Fraction of DIC with one or more lifetime passages through the soft-tissue pump normalized by its global mean ( $F_{\text{soft}} / \langle F_{\text{soft}} \rangle$ )

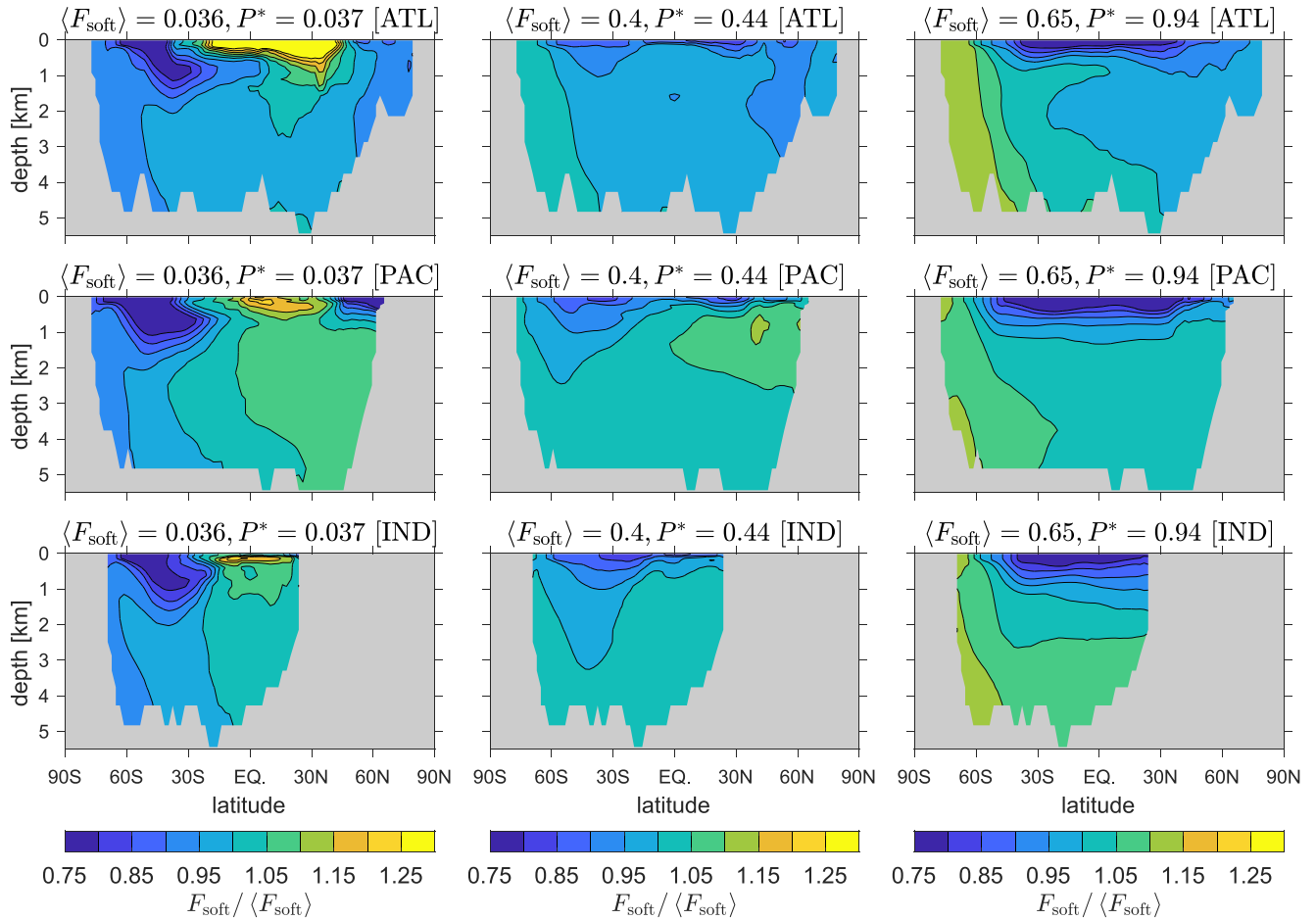


**Figure 1.** The local fraction  $F_{\text{soft}}$  of DIC that has at least one passage through the soft-tissue pump during its lifetime (residence time in the ocean), zonally averaged for each basin (top ATLantic, middle PACific, bottom INDian ocean) and normalized by its global mean value ( $\langle F_{\text{soft}} \rangle$ ) indicated in the plot titles. The middle column of plots shows the base state ( $P^* = 0.44$ ), the left column of plots shows the strongly throttled carbon pump ( $P^* = 0.037$ ), and the right column shows the strongly stimulated carbon pump ( $P^* = 0.94$ ).

## 4. Fraction of DIC Passing Through the Biological Pump and Mean Number of Lifetime Passages

### 4.1. Fraction With at Least One Lifetime Pump Passage

To summarize the highly detailed information contained in the fractions  $f_p^{n\downarrow}$  and  $f_p^{m\uparrow}$ , we first consider the fraction  $F_p$  of DIC that passes through the  $p$ -pump at least once during its residence time in the ocean (the time since entry from the atmosphere to exit back into the atmosphere, which we will refer to as the oceanic *lifetime* of carbon). Because the fraction that never passed through the pump in the past is  $f_p^{0\downarrow}$  and the fraction that will not pass through the pump in the future is  $f_p^{0\uparrow}$ , the local fraction at point  $\mathbf{r}$  that makes at least one lifetime passage through the  $p$ -pump is given by  $F_p(\mathbf{r}) = 1 - f_p^{0\downarrow}(\mathbf{r})f_p^{0\uparrow}(\mathbf{r})$ .

To quantify the large-scale spatial pattern of  $F_{\text{soft}}$ , Figure 1 shows its basin zonal averages, normalized by the global mean, for the unperturbed, weak, and strong pump states. (The normalization allows for a more quantitative comparison of the patterns as the values of  $F_{\text{soft}}$  have more than an order-of-magnitude range across the three states plotted.) The pattern of  $F_{\text{soft}}$  is shaped by the pattern of soft-pump regenerated DIC and by the degree of nutrient trapping. (For reference, Appendix B shows the corresponding basin zonal

means of regenerated DIC.) For the unperturbed state (middle column of Figure 1), the zonal-mean pattern of  $F_{\text{soft}}$  has relatively weak gradients, with the largest fractions occurring in old waters rich in regenerated DIC (upwelling equatorial waters, mid-depth North Pacific), and in the Southern Ocean. The Southern Ocean does not contain the largest concentrations of regenerated DIC, but is a region of strong nutrient trapping, which increases the probability of DIC participating in the biological pump as upwelling deep waters return regenerated DIC into a region of high productivity. The lowest values of  $F_{\text{soft}}$  are found near the surface in the subtropical gyres, where the probability of biological utilization is low and the probability of escape to the atmosphere is high.

In the global mean,  $F_{\text{soft}} \sim 40\%$  in the unperturbed state, about an order of magnitude higher than the fraction of regenerated DIC. An important factor contributing to this difference is the fact that regenerated DIC loses its identity of being regenerated (becomes preformed) as soon as it emerges into the euphotic zone, while our counting diagnostic tracks carbon throughout its lifetime until it returns to the atmosphere:  $F_p$  measures the fraction of DIC that at any point during its lifetime is regenerated at least once, regardless of whether the regenerated DIC again passes through the euphotic zone.

With the biological pump throttled down at  $P^* = 0.037$ ,  $F_{\text{soft}}$  is about an order of magnitude smaller but its pattern has sharper gradients. Southern Ocean nutrient trapping ceases as production contracts into the subtropical gyres, which leaves southern mode and intermediate waters with the lowest values of  $F_{\text{soft}}$ . The maximum values of  $F_{\text{soft}}$  lie near the tropical surface where upwelling moves what little DIC is regenerated toward the surface while the strongly weakened uptake is unable to produce much of a nutricline.

When the biological pump is cranked up at  $P^* = 0.94$ , the fraction  $F_{\text{soft}}$  increases by around 60% relative to the unperturbed state. The pattern is dominated by the influence of greatly strengthened Southern Ocean uptake and nutrient trapping as production shifts to higher latitudes. The pattern outside of the Southern Ocean has stronger vertical gradients with relatively large values of  $F_{\text{soft}}$  in deep Southern Ocean ventilated waters where DIC has the best chance of being returned to regions of high-latitude pumping.

The fraction of DIC with at least one lifetime passage through the carbonate pump (not shown) has broadly similar patterns except that the amplitude is reduced by an order of magnitude reflecting the model's globally uniform PIC/POC rain ratio of 0.07. The spatial patterns of the carbonate pump are loaded deeper into the water column with a remineralization length scale that optimized to  $\sim 4.5$  km for our model so that PIC dissolution occurs much deeper than DOC respiration.

The mean number of lifetime passages through the  $p$ -pump per DIC molecule,  $\bar{N}_p = \bar{n}_p + \bar{m}_p$ , has patterns very similar to those of  $F_p$ . A higher fraction of pump passages is associated with a greater mean number of passages, and the relation between  $\bar{N}_p$  and  $F_p$  is compact (i.e., little scatter) even at the largest perturbations considered and becomes linear in the limit of a weak pump. The reason for this is that as the pump weakens,  $F_{\text{soft}}$  is increasingly dominated by the fraction that passes through the pump only once, so that  $\bar{N}_p$  is dominated by either one passage in the past or one passage in the future. It follows that in the limit of a weak pump  $\bar{N}_p \rightarrow f_p^{1\downarrow} + f_p^{1\uparrow}$ . In this limit (see also Equation 14 below),  $F_p = f_p^{0\downarrow} f_p^{1\uparrow} + f_p^{1\downarrow} f_p^{0\uparrow} \rightarrow f_p^{1\uparrow} + f_p^{1\downarrow}$  as  $f_p^{0\downarrow}$  and  $f_p^{0\uparrow}$  both approach unity, so that  $\bar{N}_p \rightarrow F_p$ .

#### 4.2. Fraction With $N$ Pump Passages

How much of the fraction  $F_p$  with at least one lifetime  $p$ -pump passage passes through the pump two or more times? The fraction  $F_p^N$  that has exactly  $N$  lifetime passages through the  $p$ -pump can be calculated from the fractions  $f_p^{n\downarrow}$  that made  $n$  passages in the past and the fractions  $f_p^{m\uparrow}$  that will make  $m = N - n$  passages in the future:

$$F_p^N = \sum_{n=0}^N f_p^{n\downarrow} f_p^{(N-n)\uparrow}, \quad (14)$$

which holds locally at every point  $\mathbf{r}$  in the ocean. Note that  $\sum_{N=0}^{\infty} F_p^N = 1$  so that we can partition the fraction  $F_p = 1 - F_p^0$  of DIC with at least one lifetime pump passage as  $F_p = \sum_{N=1}^{\infty} F_p^N$ .

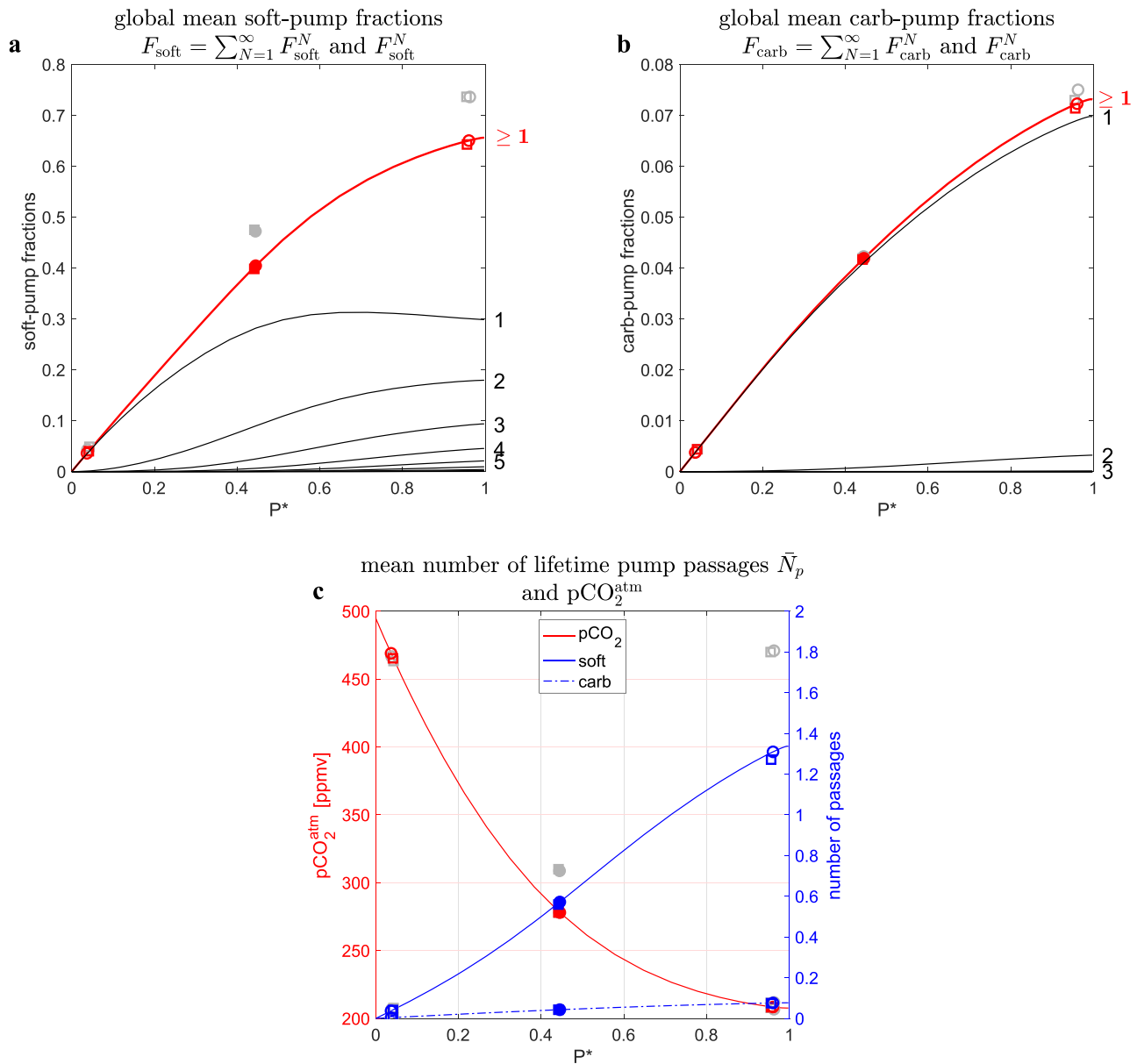


**Figure 2.** (a) The global mean fraction of DIC that passes through the soft-tissue pump during its lifetime in the ocean at least once (red curve) and exactly 1, 2, 3, ... times (black curves) as a function of  $P^*$ . (b) As (a) but for the  $\text{CaCO}_3$  pump. (c)  $\text{pCO}_2^{\text{atm}}$  (red) and the global mean number of lifetime passages  $\bar{N} = \bar{n} + \bar{m}$  through the soft-tissue pump (solid blue) and through the carbonate pump (dashed blue) as a function of  $P^*$ . The blue and red circular symbols highlight the points on the curves corresponding to the unperturbed pump with  $P^* \approx 0.44$  (filled) and to the states with  $P^* \approx 0.037$  and  $P^* \approx 0.94$  (open). For these three selected states, we also show the values obtained when using CbPM NPP data (squares), and when prescribing a respiration timescale of 1.2 years (gray symbols, circles for VGPM, and squares for CbPM). (The curves are for our best-fit case, which used VGPM NPP data and has an optimized respiration timescale of 2.5 years).

Figure 2 shows this partitioning of  $F_p$ , volume averaged over the global ocean, for both the soft and carbonate pumps as a function of  $P^*$ . When the pump is very weak, hardly any of the pumped DIC passes through the pump more than once during its lifetime. For the unperturbed VGPM base states, 40% of DIC has at least one lifetime passage through the soft-tissue pump, 28% passes through the pump exactly once, 8.8% exactly two times, 2.4% three times, and 0.8% four or more times. Put another way, 30% of the carbon that passes through the soft-tissue pump makes two or more passages. As the pump strength is increased, the fraction of DIC passing through the soft-tissue pump increases, but the fraction with exactly one lifetime passage actually decreases slightly for  $P^*$  larger than  $\sim 0.7$  as the fraction with 2, 3, or more passages

keeps increasing with pump strength. The symbols in Figure 2 for three selected states show the effect of using CbPM NPP data and of prescribing  $\kappa_{\text{doc}}^{-1} = 1.2$  years. The states optimized for a twofold shorter DOC respiration timescale of  $\kappa_{\text{doc}}^{-1} = 1.2$  years (gray symbols) have roughly 20% larger global-mean fractions. For these states, the observations constrain the POC source term  $(1 - \sigma)U_C$  and the regenerated DIC fields to be nearly invariant, but the euphotic DOC production rate,  $\sigma U_C$ , nearly doubles. (Invariance of  $(1 - \sigma)U_C$  between two states implies that their DOC production rates are in the ratio of  $\sigma_2(1 - \sigma_1)/[\sigma_1(1 - \sigma_2)]$ .) The net result is that the regeneration rate  $\kappa_{\text{doc}}[\text{DOC}]$  due to transported photosynthetic DOC (i.e., not from POC dissolution) in the upper  $\sim 500$  m increases by as much as  $\sim 80\%$  just below the euphotic zone, thereby increasing the fraction of carbon passing through the soft-tissue pump during its lifetime.

The fraction of DIC with at least one lifetime carbonate-pump passage is an order of magnitude smaller than the soft-tissue fraction, and dominated by the fraction that undergoes a single passage. For the unperturbed base state, the fraction of  $F_{\text{carb}}$  making exactly two passages is just 2%, and even for the strongest pump at  $P^* \simeq 1$  the fraction making exactly two passages is only 7.5% of  $F_{\text{carb}}$ , while the fraction with three or more passes contributes a mere 0.3% to the total. Optimizing with a fixed shorter respiration timescale has little effect on the carbonate pump because of the well-constrained PIC production rate.

Figure 2c shows the corresponding mean number of lifetime passages  $\bar{N}_p = \bar{n}_p + \bar{m}_p$  for the soft and carbonate pumps, globally volume averaged, as a function of  $P^*$ . For our best-fit case (the curves of Figure 2), the mean number of passages through the soft-tissue pump is  $\bar{N}_{\text{soft}} = 0.57$  for the base state and attains a maximum of  $\bar{N}_{\text{soft}} = 1.34$  at complete surface  $\text{PO}_4$  depletion. For the states optimized with a twofold shorter DOC respiration timescale  $\bar{N}_{\text{soft}}$  is roughly 30% larger, consistent with increased regeneration from photosynthetically produced DOC, which leads to an increase in  $F_{\text{soft}}$ . The corresponding mean number of passages through the carbonate pump is  $\bar{N}_{\text{carb}} = 0.043$  for the base state and attains a maximum of  $\bar{N}_{\text{carb}} = 0.077$  at complete surface  $\text{PO}_4$  depletion. Figure 2c also shows  $\text{pCO}_2^{\text{atm}}$ , without anthropogenic  $\text{CO}_2$ , as a function of  $P^*$ .  $\text{pCO}_2^{\text{atm}}$  is insensitive to the DOC parameter values and very similar across our four optimized variations (two NPP and two  $\kappa_{\text{doc}}$  cases). With the biological pump throttled to zero, our model produces  $\text{pCO}_2^{\text{atm}} = 493 \pm 1$  ppmv, the base-state has  $\text{pCO}_2^{\text{atm}} = 278$  ppmv (preindustrial) by construction, and at full phosphate depletion  $\text{pCO}_2^{\text{atm}}$  is drawn down to  $207 \pm 1$  ppm.

The mean number of pump passages per DIC molecule is a natural measure of the efficiency of the biological carbon pump, and we will now explore its connection with  $\text{pCO}_2^{\text{atm}}$ .

## 5. Connection With Atmospheric $\text{pCO}_2$

Here, we exploit a natural exact relation between the mean number of future  $p$ -pump passages  $\bar{m}_p(\mathbf{r}_s)$  at surface point  $\mathbf{r}_s$ , the associated globally integrated aphotic regeneration rate  $\Phi_p(\mathbf{r}_s)$ , and the one-way flux with which carbon is injected at  $\mathbf{r}_s$  into the ocean through air-sea exchange, the latter being proportional to  $\text{pCO}_2^{\text{atm}}$ . After briefly developing this relation, we recast it as a relationship between  $\bar{m}_p(\mathbf{r}_s)$  and the global mean  $p$ -pump regenerated DIC concentration by introducing the injection-tagged sequestration time  $\Gamma_p(\mathbf{r}_s)$  which is the ratio of the regenerated DIC inventory  $\mu_p(\mathbf{r}_s)$  to the globally integrated regeneration rate  $\Phi_p(\mathbf{r}_s)$  due to DIC injection at  $\mathbf{r}_s$ . We relate  $\bar{m}_p$  to the DIC inventory in this way so that we can exploit an established approximate relation (Kwon et al., 2011) between the global mean  $p$ -pump regenerated DIC inventory and  $\text{pCO}_2^{\text{atm}}$  through the buffer and alkalinity factors. This allows us to derive an equation that reveals the control of changes in  $\bar{m}_p$  and  $\Gamma_p$  on changes in atmospheric  $\text{pCO}_2^{\text{atm}}$ .

### 5.1. Linking the Number of Pump Passages to the Regenerated DIC Inventory Through the Mean Sequestration Time

The globally integrated regeneration rate of DIC that traces back to injection from the atmosphere into a given surface grid box is given by  $w^T \mathbf{R}_p \mathbf{A}^{-1} \mathbf{diag}(S_{\text{AO}})$ , where each column of  $\mathbf{diag}(S_{\text{AO}})$  is the source field for injection into a single grid box. Taking the transpose and using Equation 13, it follows that for surface point  $\mathbf{r}_s$  the globally integrated regeneration rate  $\Phi_p$  due to injection at  $\mathbf{r}_s$ , per unit injection area, is given by

$$\Phi_p(\mathbf{r}_s) = \bar{m}_p(\mathbf{r}_s) K(\mathbf{r}_s) \text{pCO}_2^{\text{atm}}, \quad (15)$$

where we have used the fact that the labeling source  $S_{AO}$  is proportional to  $p\text{CO}_2^{\text{atm}}$  from Equation 8. Equation 15 provides an exact relation locally at surface point  $\mathbf{r}_s$  between the globally integrated aphotic regeneration rate per unit area  $\Phi_p(\mathbf{r}_s)$ , the number of future passages through either the soft or carbonate pumps  $\bar{m}_p(\mathbf{r}_s)$ , the air-sea gas-exchange coefficients  $K(\mathbf{r}_s)$ , and  $p\text{CO}_2^{\text{atm}}$ . Recast as  $\bar{m}_p(\mathbf{r}_s) = \Phi_p(\mathbf{r}_s) / (K(\mathbf{r}_s)p\text{CO}_2^{\text{atm}})$ , Equation 15 shows that  $\bar{m}_p(\mathbf{r}_s)$  is an efficiency:  $\bar{m}_p(\mathbf{r}_s)$  is the globally integrated aphotic regeneration rate per unit one-way atmospheric  $\text{CO}_2$  injection rate at  $\mathbf{r}_s$ .

The regeneration rate per unit injection area  $\Phi_p$  is related to the corresponding global inventory  $\mu_p$  of  $p$ -pump regenerated DIC per unit injection area through the timescale

$$\Gamma_p(\mathbf{r}_s) = \mu_p(\mathbf{r}_s) / \Phi_p(\mathbf{r}_s) . \quad (16)$$

We call  $\Gamma_p(\mathbf{r}_s)$  the injection-tagged sequestration time because it is the mean time that the regenerated DIC that results from injection into the ocean at  $\mathbf{r}_s$  (“injection-tagged”) remains in the aphotic zone.  $\Gamma_p(\mathbf{r}_s)$  can be calculated directly from the decay response to a unit (injection-tagged) regeneration source, or equivalently by calculating the global inventory  $\mu_p$  and using Equation 16.

To calculate  $\mu_p$ , we note that the  $p$ -pump regeneration response  $\chi_p^{\text{reg}}$  to surface source  $S_{AO}$  at each surface pixel satisfies

$$\mathbf{T}\chi_p^{\text{reg}} = \mathbf{R}_p\mathbf{A}^{-1}\mathbf{diag}(S_{AO}) - \mathbf{L}_a\chi_p^{\text{reg}} , \quad (17)$$

where  $\mathbf{A}$  is the carbon-cycle system operator for the labeling tracers (cf., Equation 9),  $\mathbf{R}_p$  is the  $p$ -pump regeneration operator (cf., Equation 10), and  $\mathbf{L}_a$  enforces the boundary condition of zero regenerated DIC in the euphotic zone by clamping  $\chi_p^{\text{reg}}$  to zero in the euphotic zone through fast relaxation (any tracer in the euphotic zone is by definition preformed). ( $\mathbf{L}_a$  is a diagonal operator with nonzero elements of  $1/\tau_a$  only in the euphotic zone; we use  $\tau_a = 10$  s, but there is no sensitivity to the precise value of  $\tau_a$ .) Here,  $\mathbf{T}$  is the discretized version of the advection-diffusion transport operator  $\mathcal{T}$  replicated (for consistent notation throughout) four times to act on the labeling tracers for each carbon species (DIC, DOC, PIC, and POC), which are organized into  $\chi$  (formally if  $\mathbf{T}_1$  is the discretized advection-diffusion operator  $\mathcal{T}$ , then  $\mathbf{T} = \mathbf{I}_4 \otimes \mathbf{T}_1$ , where  $\mathbf{I}_4$  is the  $4 \times 4$  identity matrix). The corresponding injection-tagged globally integrated inventories per unit injection area,  $\mu_p = \mathbf{diag}^{-1}(a_s)\chi_p^{\text{reg},T}w$ , where  $a_s$  is the vector of surface areas, are efficiently computed by solving Equation 17 for  $\chi_p^{\text{reg}}$  and taking the transpose to obtain

$$\mu_p = \mathbf{diag}^{-1}(a_s)\mathbf{diag}(S_{AO})\mathbf{W}\tilde{\mathbf{A}}^{-1}\tilde{\mathbf{R}}_p(\tilde{\mathbf{T}} + \mathbf{L}_a)^{-1}u . \quad (18)$$

With  $\mu_p$  known, and  $\Gamma_p$  given by Equation 16, we can now rewrite  $\mu_p = \Gamma_p \Phi_p$  using Equation 15 as

$$\mu_p(\mathbf{r}_s) = \Gamma_p(\mathbf{r}_s)\bar{m}_p(\mathbf{r}_s)K(\mathbf{r}_s)p\text{CO}_2^{\text{atm}} , \quad (19)$$

which in terms of the global-mean  $p$ -pump regenerated DIC concentration  $C_p^{\text{reg}} \equiv (1/V_O)\int d^2r_s\mu_p(\mathbf{r}_s)$ , where  $V_O$  is the global ocean volume, becomes

$$\begin{aligned} C_p^{\text{reg}} &= \frac{1}{V_O}p\text{CO}_2^{\text{atm}} \int d^2r_s \bar{m}_p(\mathbf{r}_s)\Gamma_p(\mathbf{r}_s)K(\mathbf{r}_s) , \\ &= \frac{1}{z_O}p\text{CO}_2^{\text{atm}} \langle \bar{m}_p \rangle_{\Gamma K} \langle \Gamma_p \rangle_K \langle K \rangle , \end{aligned} \quad (20)$$

where  $z_O$  is the mean depth of the ocean ( $V_O$  divided by the global sea-surface area). The second line of Equation 20 re-expresses the surface integral of the product  $\bar{m}_p(\mathbf{r}_s)\Gamma_p(\mathbf{r}_s)K(\mathbf{r}_s)$  as a product of three weighted surface averages, which makes it simpler to deal with this expression in subsequent analysis. In Equation 20, the notation  $\langle X_W \rangle$  stands for the  $W$ -weighted surface average of quantity  $X$  defined as usual as  $\langle X_W \rangle \equiv \int d^2r_s X(\mathbf{r}_s)W(\mathbf{r}_s) / \int d^2r_s W(\mathbf{r}_s)$ . Thus,  $\langle \bar{m}_p \rangle_{\Gamma K}$  is the surface average of  $\bar{m}_p(\mathbf{r}_s)$  weighted by the pattern of the product  $\Gamma(\mathbf{r}_s)K(\mathbf{r}_s)$ , the quantity  $\langle \Gamma_p \rangle_K$  is the surface average of the injection-tagged seques-

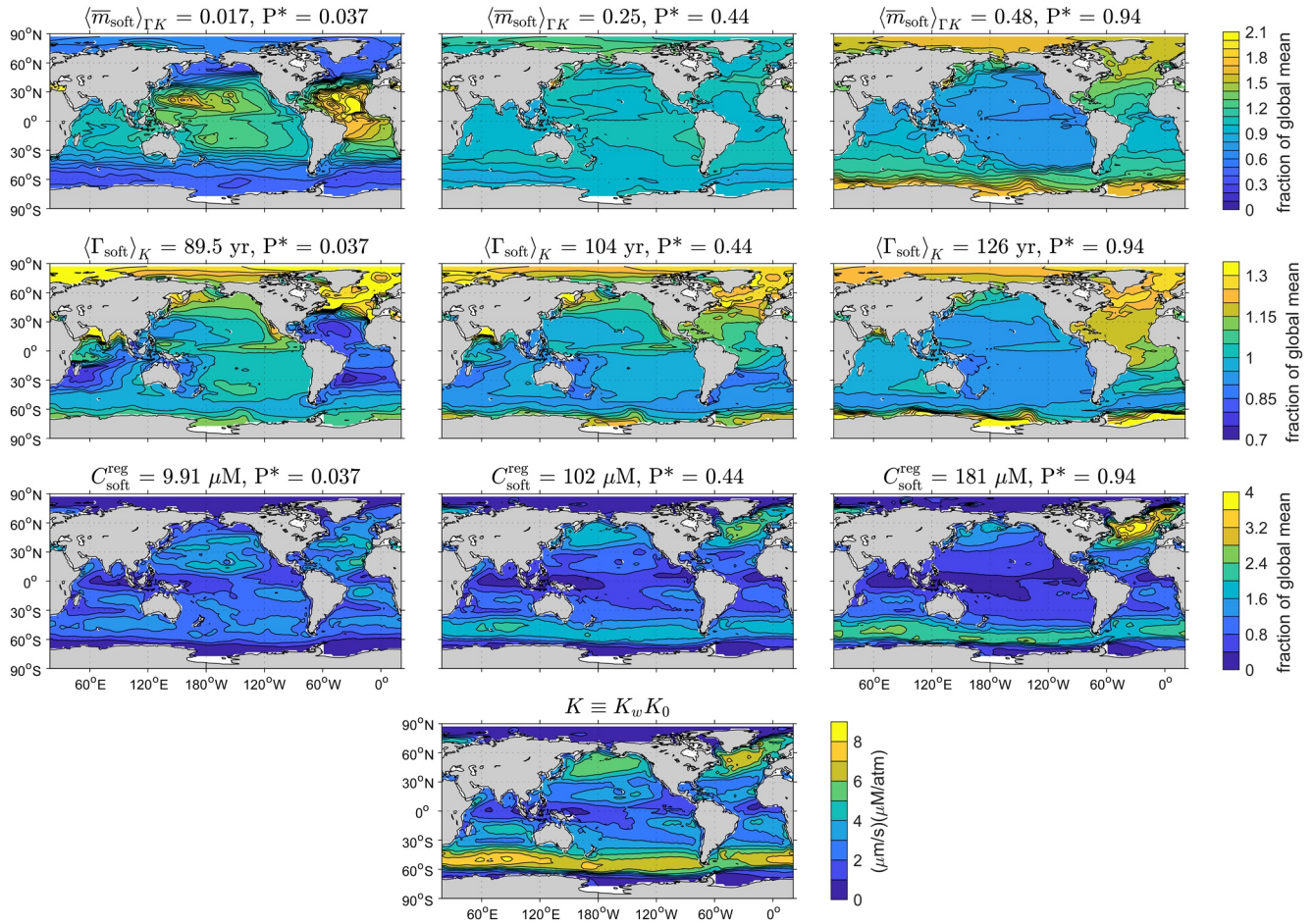


**Figure 3.** Top row of plots: The mean number of future passages  $\bar{m}_{\text{soft}}$  through the soft-tissue carbon pump at the sea surface, normalized by its  $KT_{\text{soft}}$ -weighted surface mean, whose value is given in the plot title. Second row of plots: The mean injection-tagged sequestration time  $\Gamma_{\text{soft}}$  of DIC, normalized by its  $K$ -weighted surface mean, whose value is given in the plot title. Third row of plots: The soft-pump injection-tagged regenerated DIC inventory per unit area  $\mu_{\text{soft}}$  due to CO<sub>2</sub> injection at a given surface location, normalized using the global-mean soft-pump regenerated DIC concentration  $C_{\text{soft}}^{\text{reg}}$  indicated in the plot titles. The middle column of plots shows the base state ( $P^* = 0.44$ ), the left column of plots shows the strongly throttled carbon pump ( $P^* = 0.037$ ), and the right column shows the strongly stimulated carbon pump ( $P^* = 0.94$ ). Bottom: Map of the product of piston velocity and CO<sub>2</sub> solubility  $K_w K_0$  (independent of  $P^*$ ).

tration time  $\Gamma_p(\mathbf{r}_s)$  weighted by the air-sea exchange coefficients  $K(\mathbf{r}_s)$ , and  $\langle K \rangle$  is simply the unweighted surface average of  $K(\mathbf{r}_s)$  (i.e., weight  $W = 1$ ).

## 5.2. Surface Distributions of Mean Number of Future Pump Passages, Injection-Tagged Mean Sequestration Time, and Regenerated DIC Inventory

Equation 20 provides the crucial link between the  $p$ -pump regenerated global mean DIC concentration  $C_p^{\text{reg}}$  and the number of future  $p$ -pump passages via the injection-tagged mean sequestration time  $\Gamma_p$ . While Equation 20 is exact, it does not directly reveal the control of the number of pump passages on  $\text{pCO}_2^{\text{atm}}$  because pump perturbations cause fractional changes in  $C_p^{\text{reg}}$  that are of the same order of magnitude as the fractional changes in  $\langle \bar{m}_p \rangle_{\Gamma K}$ . Before developing a more direct relation, it is instructive to examine the surface fields that enter expression (20). The number of pump passages per molecule following surface injection,  $\bar{m}_p(\mathbf{r}_s)$ , is a local metric of  $p$ -pump efficiency and these fields are key ingredients of further analysis.

The top plots of Figure 3 show maps of  $\bar{m}_{\text{soft}}$  at the surface normalized by its global mean to allow comparison of the patterns across three selected states of the biological pump (weak, unperturbed, strong). For

the unperturbed state,  $\bar{m}_{\text{soft}}$  has little spatial variation around its surface average of about 0.26, which from Equation 19 means that the injection-tagged regenerated carbon inventory  $\mu_{\text{soft}}$  and  $\Gamma K$  have similar patterns as verified below. For the strong-pump case at  $P^* = 0.94$ , the surface average nearly doubles and the pattern of  $\bar{m}_{\text{soft}}$  becomes enhanced at high latitudes as maximum production and pumping are shifted poleward. The increased production of biogenic particles in the high-latitude nutrient trapping regions increases the number of times carbon becomes available as DIC for carbon fixation and subsequent export. For throttled biological uptake,  $\bar{m}_{\text{soft}}$  approaches zero and its pattern reverses with the collapse of high-latitude production as the nutrient distribution becomes homogeneous. Thus, for throttled uptake, the pattern of  $\bar{m}_{\text{soft}}$  has its maxima in the subtropical gyres and broadly mirrors the pattern of the throttled production.

The second row of Figure 3 shows maps of the injection-tagged mean sequestration times  $\Gamma_{\text{soft}}$ , normalized by their global means to highlight changes in pattern. Note that the injection-tagged mean sequestration time differs in definition from that examined by DeVries et al. (2012), where the sequestration time was tagged by the location where the regeneration occurred (“regeneration-tagged”). (Their phosphate-only model had no dissolved organic pool so that regeneration and uptake were horizontally co-located.) The pattern of the soft-pump regeneration-tagged sequestration time has an order-of-magnitude dynamic range and is highly localized in the deep-water formation regions of the Weddell Sea, Antarctic coast, and sub-polar North Atlantic, where these times exceed several centuries (see Appendix C for plots of the regeneration-tagged sequestration times for our model). The regeneration-tagged sequestration time changes little with uptake pattern for our model because the sequestration time is dominated by deep POC-flux-driven remineralization, there is no geographic variation in particle-flux profiles, and the regeneration-tagged sequestration time is determined by the locally normalized regeneration rate. By contrast, the injection-tagged  $\Gamma_{\text{soft}}$  is determined by the normalized regeneration rate due to carbon that traces back to a given surface point of injection from the atmosphere. The pattern of the injection-tagged  $\Gamma_{\text{soft}}$  is thus much more smoothed out with about threefold smaller maxima and only a factor-of-two dynamic range. This is because DIC can be transported quite far from its injection site before participating in the biological pump, which has the effect that DIC injected at a given surface point is utilized and regenerated over a wide region. This reduces the maximum mean sequestration times associated with the injection site, while at the same time increasing the region of influence of deep-water formation regions. Changing the pump strength changes the global mean injection-tagged sequestration time from 90 years at  $P^* = 0.037$  to 126 years at  $P^* = 0.94$  as production moves poleward and injected DIC has increased access to deep-water formation regions. The patterns of  $\Gamma_{\text{soft}}$  also undergo modest changes. Increased pump strength and poleward shifted production lead to an increase in  $\Gamma_{\text{soft}}$  relative to the global mean near Antarctica where long-residence-time bottom water is formed. Decreased pump strength leads to relative reductions of  $\Gamma_{\text{soft}}$  in the Atlantic, Indian, and North-Pacific subtropical gyres. DIC injection into the subtropical gyres is now more likely to be pumped in the gyres than in deep-water formation regions, causing a relative (to the global mean) reduction of  $\Gamma_{\text{soft}}$  in the subtropics.

The third row of Figure 3 shows maps of the injection-tagged global inventory  $\mu_{\text{soft}}$  of respired (soft-pump regenerated) DIC per unit injection area. To allow comparison of the patterns, these fields have again been normalized by their global means. For the unperturbed base state, the pattern of  $\mu_{\text{soft}}$  reflects the pattern of atmospheric DIC injection ( $K_0 K_w$ , bottom plot of Figure 3), which is dominated by the piston velocity  $K_w$  and mirrors the amplitude of surface wind stress with subpolar maxima (storm tracks) and secondary maxima in the nonequatorial tropics (trades). As the strength of the pump is varied, the pattern of  $\mu_{\text{soft}}$  is modulated by the changed pattern of production. For the throttled pump high-latitude DIC injection leads to a relatively reduced inventory because of the collapse of nearby production, while for the cranked-up pump, high-latitude DIC injection leads to relatively larger inventories because of the relative increase of high-latitude production.

The corresponding fields of the carbonate pump have much smaller amplitudes (quantified below), but the patterns of  $\bar{m}_{\text{carb}}$  and  $\mu_{\text{carb}}$  are very similar to their soft-tissue counterparts. However, the patterns of  $\Gamma_{\text{carb}}$  are very different because of the deep dissolution of  $\text{CaCO}_3$ . (The patterns of the injection-tagged  $\Gamma_{\text{carb}}$  are plotted in Appendix C together with their regeneration-tagged counterpart.) Carbonate dissolved in the slowly ventilated deep Pacific thus leads to order-1000-year sequestration times (longest in the western North Pacific), while carbonate dissolved in the more rapidly ventilated deep Atlantic has a sequestration time of only roughly 600 years, with the Indian Ocean being intermediate. DIC injected into the Pacific has

access to the dissolution region with the longest sequestration times and the injection-tagged sequestration time is hence longest in the Pacific. For the state with the throttled pump, the sequestration times are a few percent *longer* in the North Pacific as the gyre-contracted production now better matches the regions where dissolved calcium carbonate has the longest sequestration times. For the states with the strengthened pump, the poleward intensified production pattern gives DIC injected in the Pacific access to regeneration regions with lower sequestration times reducing the injection-tagged sequestration times by order 10%.

### 5.3. Systematic Dependence of $\langle \bar{m}_p \rangle_{\Gamma_K}$ , $C_p^{\text{reg}}$ , and $\langle \Gamma_p \rangle_K$ on Pump Strength $P^*$

Figure 4 shows the (weighted) surface means that enter Equation 20 for the global mean regenerated DIC concentrations as a function of  $P^*$ . Both the mean number of future passages through the soft-tissue and carbonate pumps,  $\langle \bar{m}_{\text{soft}} \rangle_{\Gamma_K}$  and  $\langle \bar{m}_{\text{carb}} \rangle_{\Gamma_K}$ , increase monotonically from zero at  $P^* = 0$  until they reach their maximum values of 0.50 and 0.021 at complete  $\text{PO}_4$  utilization ( $P^* = 1$ ). The ratio  $\langle \bar{m}_{\text{carb}} \rangle_{\Gamma_K} / \langle \bar{m}_{\text{soft}} \rangle_{\Gamma_K}$  has a value of roughly 0.045, which is set by the rain ratio  $R$ , but is less than  $R = 0.069$ . This is consistent with the low  $\text{CaCO}_3$  production rate making it much less likely for carbonate-pump regenerated DIC to pass through the carbonate pump again (i.e.,  $F_{\text{carb}} \approx F_{\text{carb}}^1$ , see also Figure 2).

The global mean regenerated DIC concentrations,  $C_{\text{soft}}^{\text{reg}}$  and  $C_{\text{carb}}^{\text{reg}}$ , similarly increase monotonically with  $P^*$ . The fact that these curves are not straight lines is due to the model's variable C:P uptake stoichiometry. As phosphate uptake and  $P^*$  increase,  $dC_{\text{soft}}^{\text{reg}} / dP^*$  decreases because as production shifts poleward it occurs at lower C:P. This effect is exaggerated for the carbonate pump presumably because (at least in our model) the carbonate pump always regenerates in deep waters and therefore has less regenerated DIC inventory to gain to offset reduced C:P by moving production poleward toward deep-water formation regions.

The global mean injection-tagged sequestration time for the soft-tissue pump increases monotonically from about 90 years near zero pump strength to about 130 years for the strongest pump. This behavior is due to the poleward migration of the uptake, which makes surface injected DIC more accessible to regeneration where deep waters are formed. As noted in the discussion of the patterns above, the same dynamics have the opposite effect on the carbonate pump's injection-tagged sequestration time. As the pump strength is turned down and production contracts into the subtropics, injection in the Pacific preferentially accesses regeneration in the western tropical Pacific, which leads to the longest sequestration times (see also Appendix C). However, this effect is relatively small with  $\langle \Gamma_{\text{carb}} \rangle_K$  ranging only from roughly 650–685 years across the entire perturbation range.

The ratio  $C_{\text{carb}}^{\text{reg}} / C_{\text{soft}}^{\text{reg}}$  decreases from about 0.4 to 0.2 (0.3 for the base state) over the range of  $P^*$ . This is much larger than the rain ratio because of the much longer sequestration times of DIC regenerated from PIC dissolution. As  $P^*$  increases, the injection-tagged sequestration time of the soft-tissue pump increases, while that of the carbonate pump decreases leading to a decrease of  $C_{\text{carb}}^{\text{reg}} / C_{\text{soft}}^{\text{reg}}$ .

The differences between the fully optimized states and those for which we fixed  $\kappa_{\text{doc}}^{-1} = 1.2$  years are small for the carbonate pump metrics where they are on the same order as the VGPM versus CbPM differences.  $C_{\text{soft}}^{\text{reg}}$  and  $C_{\text{carb}}^{\text{reg}}$  are both insensitive to state, which indicates that they are well constrained by the observations. (Zonal means of regenerated DIC for the different states are also nearly indistinguishable.) The surface averaged mean number of future passages  $\langle \bar{m}_{\text{soft}} \rangle_{\Gamma_K}$  through the soft-tissue pump is roughly 20% larger for the states optimized for a faster respiration timescale of  $\kappa_{\text{doc}}^{-1} = 1.2$  years, similar to what was seen for the global mean number of lifetime passages in Figure 2. With  $C_{\text{soft}}^{\text{reg}}$  being nearly invariant, larger  $\langle \bar{m}_{\text{soft}} \rangle_{\Gamma_K}$  must be accompanied by smaller mean sequestration time  $\Gamma_{\text{soft}K}$  because  $C_{\text{soft}}^{\text{reg}} \propto \langle \Gamma_{\text{soft}} \rangle_K \langle \bar{m}_{\text{soft}} \rangle_{\Gamma_K}$  as can be verified from Figure 4.

### 5.4. Control of $\text{pCO}_2^{\text{atm}}$ by the Number of Pump Passages and Injection-Tagged Sequestration Time

In an extension of the theory of Ito and Follows (2005) to include the carbonate pump, Kwon et al. (2011) developed an approximate relation for the fractional changes in  $\text{pCO}_2^{\text{atm}}$  of the form

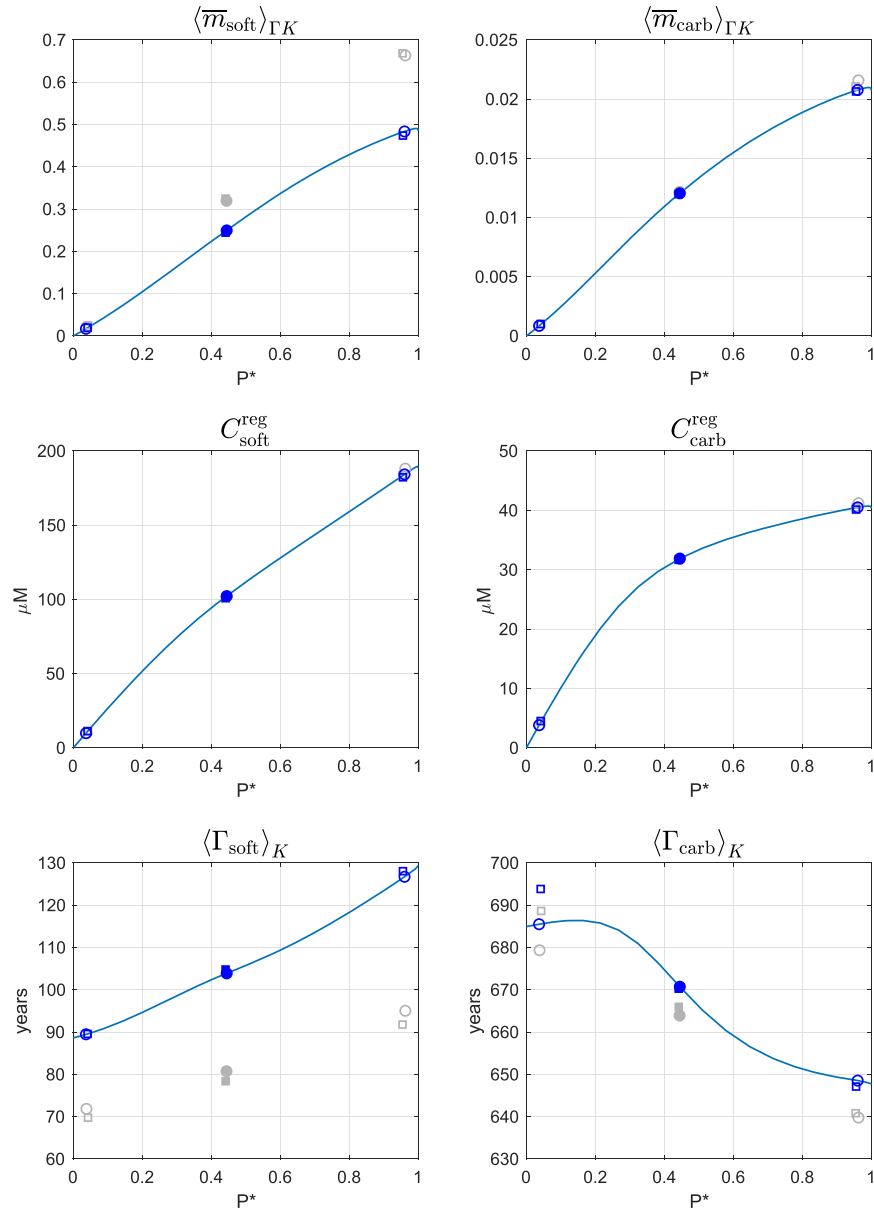


**Figure 4.** The systematic dependence of the quantities controlling  $\text{pCO}_2^{\text{atm}}$  as a function of  $P^*$ : The  $\Gamma K$ -weighted surface average of the mean number of future pump passages  $\langle \bar{m}_{\text{soft}} \rangle_{\Gamma K}$  and  $\langle \bar{m}_{\text{carb}} \rangle_{\Gamma K}$  (top plots), the global volume averaged regenerated DIC concentrations  $C_{\text{soft}}^{\text{reg}}$  and  $C_{\text{carb}}^{\text{reg}}$  (middle plots), and the  $K$ -weighted surface average of the mean sequestration times  $\langle \Gamma_{\text{soft}} \rangle_K$  and  $\langle \Gamma_{\text{carb}} \rangle_K$  (bottom plots). The blue circles highlight the points on the curves corresponding to the unperturbed pump with  $P^* \approx 0.44$  (filled) and to the states with  $P^* \approx 0.037$  and  $P^* \approx 0.94$  (open). For these three highlighted states, we also show the values obtained when using CbPM NPP data (squares), and when prescribing a respiration timescale of 1.2 years (gray symbols, circles for VGPM and squares for CbPM). (The states comprising the curves have the biogeochemical parameters of our best-fit case, which used VGPM NPP data and has an optimized respiration timescale of 2.5 years).

$\delta \text{pCO}_2^{\text{atm}} / \text{pCO}_2^{\text{atm}} = \mathcal{R}_s \delta C_{\text{soft}}^{\text{reg}} + \mathcal{R}_c \delta C_{\text{carb}}^{\text{reg}}$ , where  $\mathcal{R}_s$  and  $\mathcal{R}_c$  are simple functions of global mean preformed DIC ( $C^{\text{pre}}$ ), global mean preformed TA ( $A^{\text{pre}}$ ), and suitable surface means of the Revelle buffer factor  $\mathcal{R}_c$  and the alkalinity factor  $\mathcal{R}_s$ . Appendix D sketches a derivation of that relation to be explicit about the assumptions and shows that using Equation 20 to express infinitesimal changes in the global mean regenerated

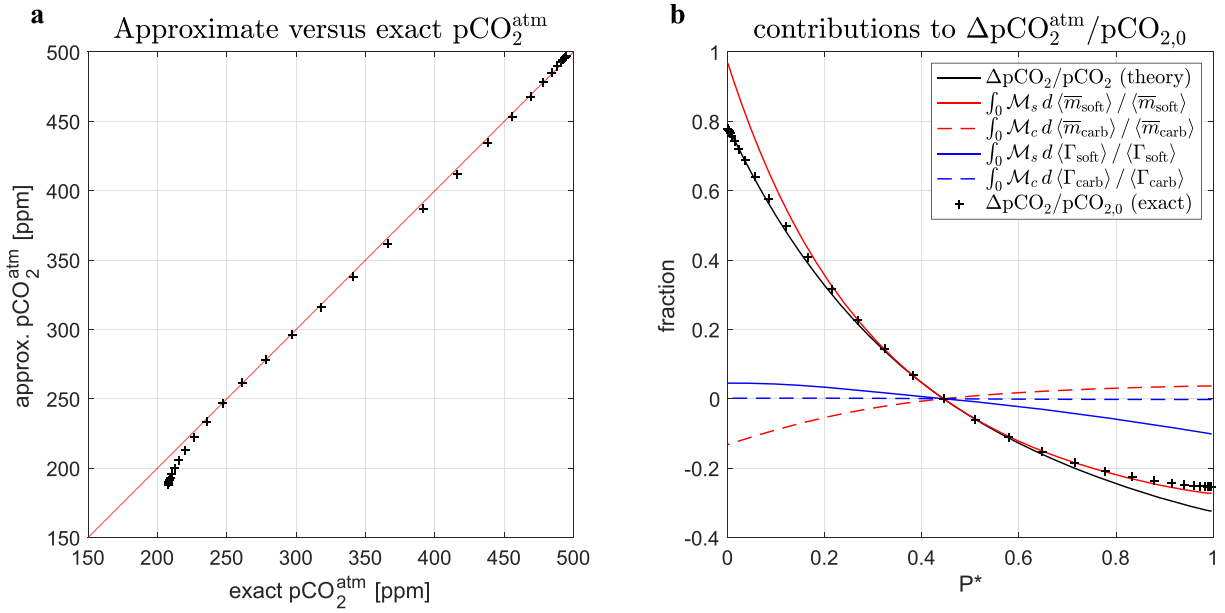


**Figure 5.** (a) pCO<sub>2</sub><sup>atm</sup> as predicted by integrating Equation 21 versus the “exact” model solutions, that is, the solutions for pCO<sub>2</sub><sup>atm</sup> from the full carbon-cycle model. (b) The corresponding fractional change ΔpCO<sub>2</sub><sup>atm</sup> / pCO<sub>2,0</sub><sup>atm</sup> from the unperturbed base-state value of pCO<sub>2,0</sub><sup>atm</sup> = 278 ppmv and the contributions from each term of the integrand as indicated in the legend.

DIC concentrations in terms of infinitesimal changes in the mean number of future pump passages, one obtains the differential equation

$$\frac{\delta p\text{CO}_2}{p\text{CO}_2} = \mathcal{M}_s \left( \frac{\delta \langle \bar{m}_{\text{soft}} \rangle_{\Gamma_K}}{\langle \bar{m}_{\text{soft}} \rangle_{\Gamma_K}} + \frac{\delta \langle \Gamma_{\text{soft}} \rangle_K}{\langle \Gamma_{\text{soft}} \rangle_K} \right) + \mathcal{M}_c \left( \frac{\delta \langle \bar{m}_{\text{carb}} \rangle_{\Gamma_K}}{\langle \bar{m}_{\text{carb}} \rangle_{\Gamma_K}} + \frac{\delta \langle \Gamma_{\text{carb}} \rangle_K}{\langle \Gamma_{\text{carb}} \rangle_K} \right), \quad (21)$$

where  $\mathcal{M}_s$  and  $\mathcal{M}_c$  are functions of  $R_C, R_A, C^{\text{pre}}, C_{\text{soft}}^{\text{reg}}, C_{\text{carb}}^{\text{reg}}$ , and  $A^{\text{pre}}$ .

Equation 21 can be integrated from the unperturbed state to predict pCO<sub>2</sub><sup>atm</sup> for the states with a perturbed biological pump. Specifically, denoting the right-hand side of Equation 21 as δRHS and the unperturbed base-state value of pCO<sub>2</sub><sup>atm</sup> by pCO<sub>2,0</sub><sup>atm</sup>, with ΔpCO<sub>2</sub><sup>atm</sup> ≡ pCO<sub>2</sub><sup>atm</sup> – pCO<sub>2,0</sub><sup>atm</sup>, one has from direct integration of both sides of Equation 21 that ΔpCO<sub>2</sub><sup>atm</sup> / pCO<sub>2,0</sub><sup>atm</sup> = (exp ∫<sub>0</sub><sup>1</sup> δRHS – 1). We perform this integral numerically by evaluating all the terms of the right-hand side of Equation 21 for each of our suite of roughly 40 states, with the δ changes for each state approximated by the finite difference between a given state and an adjacent slightly perturbed state for which the uptake-rate coefficients have been increased by 1%. (In practice, it is convenient to use P\* as the integration variable, that is, for any quantity X the change δX is replaced by (δX/δP\*)dP\*, the resulting integrand is interpolated to a uniform P\* grid, and the dP\* integral runs from P\* at the unperturbed state to the P\* of the state for which pCO<sub>2</sub><sup>atm</sup> is to be calculated.) The buffer and alkalinity factors, R<sub>C</sub> and R<sub>A</sub>, that enter the integrand through  $\mathcal{M}_s$  and  $\mathcal{M}_c$  were calculated as functions of surface DIC and TA only using simplified expressions that approximate DIC by the sum of bicarbonate and carbonate ions only and TA by carbonate alkalinity (Sarmiento & Gruber, 2006). We obtain the best fit of the theoretically calculated pCO<sub>2</sub><sup>atm</sup> from Equation 21 to the full model’s solution for pCO<sub>2</sub><sup>atm</sup> if we use the K-weighted surface average of DIC and TA to calculate R<sub>C</sub> and R<sub>A</sub> and additionally scale up R<sub>C</sub> by a factor of 1.034. (The empirical scale factor improves the fit by about 1%.)

Figure 5a shows the comparison of pCO<sub>2</sub><sup>atm</sup> predicted from Equation 21 with the model-computed (“exact”) pCO<sub>2</sub><sup>atm</sup>. For the states with a weakened pump the predictions lie within 1% of the values computed by our

model. For the states with a strengthened pump, the error remains below 5% for  $P^* < 0.85$ , or equivalently for  $p\text{CO}_2^{\text{atm}} > 214$  ppm, and increases to about 9% at complete surface  $\text{PO}_4$  depletion. To obtain a yet better fit presumably requires relaxing the various approximations made. However, because the fit is already quite good and the main point of Equation 21 is to illustrate that changes in the number of soft-tissue pump passages exert a leading control on  $p\text{CO}_2^{\text{atm}}$ , we do not pursue a more accurate theory here. The contributions to  $\Delta p\text{CO}_2^{\text{atm}} / p\text{CO}_{2,0}^{\text{atm}}$  from the four terms on the RHS of Equation 21 are shown in Figure 5b. The contributions from  $\langle \Gamma_{\text{carb}} \rangle_K$  are negligible, and the contributions from  $\langle \Gamma_{\text{soft}} \rangle_K$  and  $\langle \bar{m}_{\text{carb}} \rangle_{\Gamma K}$  partially cancel each other, leaving  $\langle \bar{m}_{\text{soft}} \rangle_{\Gamma K}$  as the dominant control on  $p\text{CO}_2^{\text{atm}}$  for the perturbations considered here, which leave the circulation unchanged. The degree of this control can be quantified in terms of the dimensionless sensitivity of fractional changes in  $p\text{CO}_2^{\text{atm}}$  to fractional changes in  $\langle \bar{m}_{\text{soft}} \rangle_{\Gamma K}$ . For the unperturbed base state, this sensitivity to changes in the soft-tissue pump is  $\partial \log(p\text{CO}_2^{\text{atm}}) / \partial \log(\langle \bar{m}_{\text{soft}} \rangle_{\Gamma K}) = -0.411 \pm 0.002$ , that is, a 1% increase in  $\langle \bar{m}_{\text{soft}} \rangle_{\Gamma K}$  results in a 0.4% reduction in  $p\text{CO}_2^{\text{atm}}$ . The corresponding sensitivity to changes in the carbonate pump is  $\partial \log(p\text{CO}_2^{\text{atm}}) / \partial \log(\langle \bar{m}_{\text{carb}} \rangle_{\Gamma K}) = +0.0710 \pm 0.0001$ , which is nearly 6 times smaller and of opposite sign.

## 6. Discussion

We have explored the mean number of carbon passages through the soft-tissue and carbonate pumps per DIC molecule as natural metrics of the efficiency of the biological pump. Because these metrics track carbon through its entire lifetime in the ocean from injection by air-sea exchange to outgassing back into the atmosphere, the global mean fraction of DIC that undergoes at least one lifetime passage through the biological pump is an order of magnitude larger than the global mean fraction of regenerated DIC. Our metrics are computed directly for carbon and are hence not affected by the regionally varying C:P stoichiometry of organic-matter production that decouples the carbon and phosphate pumps (Galbraith & Martiny, 2015; Teng et al., 2014) and complicates the interpretation of phosphate-based metrics of pump efficiency. However, deviations of C:P from the Redfield value are large only regionally, and the effects of the regional decoupling are likely to be modest for globally integrated quantities. Indeed, our simple model with spatially varying C:P stoichiometry produces a sensitivity of  $dp\text{CO}_2/dP^* = -285 \pm 4$  ppmv for the unperturbed base state, which is within about 10% of the theoretical estimate of  $-312$  ppmv by Ito and Follows (2005), and the C:P ratio of globally integrated exported organic matter is  $108.3 \pm 0.6$ , which is close to the canonical Redfield value of 106.

We examined the unperturbed base state of the biological pump constrained by observations as well as a suite of idealized perturbations that sweep out states with near-zero production concentrated in the subtropical gyres to nearly complete nutrient utilization with poleward intensified production. There is little sensitivity in both the theoretical and modeled  $p\text{CO}_2^{\text{atm}}$  to the value of the respiration timescale across our suite of optimized states in part because the *fractional* changes involved are less sensitive to the DOC source/sink parameters and in part because of cancellation between changes in the number of pump passages and changes in the sequestration times. For realistic perturbations of biological production driven by, for example, changes in dissolved iron availability, the sensitivities of  $p\text{CO}_2^{\text{atm}}$  to changes in the number of pump passages may be different than those calculated here depending on the detailed pattern of the productivity changes. The future biological pump will also respond to changes in the physical circulation such as decreased ventilation driven by increased surface stratification and reduced large-scale overturning, and for such perturbations, the changes in the mean sequestration time are likely to play a much more prominent role.

It is worth emphasizing what constitutes a “passage” through the soft-tissue pump in our analysis. Carbon in a DIC molecule is counted as making a passage through the soft-tissue pump if that carbon contributes to DOC respiration in the aphotic zone (in the past, future, or both depending on the metric). Semi-labile DOC in our model is produced both from the dissolution of organic particles and directly during production in the euphotic zone. The soft-tissue pump here thus comprises both the physical transport of DOC from the euphotic zone into the interior and the POC particle transport followed by dissolution. At the expense of additional complexity, one could partition DIC according to how much is pumped by each pathway but that is beyond the scope of this paper. Because both pathways are involved, the mean number of passages through

the soft-tissue pump and the corresponding injection-tagged mean sequestration times showed order 30% sensitivity to a factor-of-two change in the respiration timescale when all other parameters are optimized. The passage-based metrics of pump efficiency thus better reflect the state of the biological pump than just the regenerated inventories, the latter being insensitive to the details of the DOC pathways. By including labile and refractory DOC pools and constraining the carbon model with DOC observations (e.g., DeVries & Weber, 2017; Roshan & DeVries, 2017) it might be possible to better constrain the role of DOC production, and possibly also DOC consumption by nutrient-starved phytoplankton (e.g., Bronk et al., 2007), in driving pump efficiency.

As for any modeling study, there are a number of caveats to keep in mind. To limit complexity, the biogeochemical parameters of our model were globally uniform, POC and POP had the same flux profiles, and DOC and DOP had identical remineralization timescales. In the real ocean, most of these parameters vary spatially (for variations in flux profiles, see, e.g., Honda, 2020; Marsay et al., 2015; Weber et al., 2016), and there is evidence that  $\text{PO}_4$  is remineralized preferentially relative to carbon (Letscher & Moore, 2015). The remineralization rate of  $\text{CaCO}_3$  also depends on the saturation state of seawater with respect to crystalline  $\text{CaCO}_3$  and a globally uniform PIC remineralization length scale is a simplifying approximation. Some of these limitations could be relaxed by including two or more particle-size classes, carrying oxygen and specifying oxidation rates rather than profile parameters, and PIC dissolution could be keyed to  $\text{CaCO}_3$  saturation, although the details of how best to parameterize dissolution are still debated (Battaglia et al., 2016). We have neglected all carbon export that is not due to sinking particles and DOC transport, such as export by diurnally migrating zooplankton (e.g., Ducklow et al., 2001), all external sources of nutrients and alkalinity, terrestrial sources of carbon, and all sinks due to sediment burial. We have also used a steady circulation so that we cannot resolve any seasonal covariances between biology and circulation. While these caveats are important, it is equally important to remember that the point here was not to produce a detail-rich mechanistic model of the carbon cycle, but to demonstrate the character and potential of using the number of pump passages as a metric of carbon-pump efficiency. By optimizing the parameters of our simple model, we match the observed annual-mean  $\text{PO}_4$ , DIC, and TA fields with a quadratic model-observation mismatch that is only about 6% of the spatial variance. This fidelity to the observed fields can be regarded as justification for many of the approximations made. Conversely, a more mechanistic model typically requires more parameters, not all of which may be constrainable through optimization against available data.

A related caveat is that our findings are based on a single modeling framework. While the conceptual content of our work and the theoretical relationships developed here are independent of model details, there is of course inherent uncertainty in all quantitative findings when using a single model. Although we investigated some parametric uncertainties (respiration timescale and NPP data used in the uptake parameterization), structurally different models, different circulations and spatial resolutions, or a more mechanistic representation of phytoplankton physiology, inclusion of grazing and vertical zooplankton migration, all have the potential to impact our quantitative results. It will therefore be very useful to explore the metrics and relationships explored here for other models and circulations in future research. Passage-number diagnostics of the biological pump can straightforwardly be calculated for models whose transport is cast in matrix form. The transport matrices used here were obtained through data assimilation (see also, John et al., 2020), but they can also be constructed for climate models (e.g., Chamberlain et al., 2019; Holzer et al., 2020; Kvale et al., 2017).

A largely observation-based estimate of the global mean number of future soft-tissue-pump passages at the surface,  $\langle \bar{m}_{\text{soft}} \rangle_{\Gamma K}$ , may also be possible. Three out of four of the ingredients that determine  $\langle \bar{m}_{\text{soft}} \rangle_{\Gamma K}$  (cf. Equation 20) are directly available from observations:  $\text{pCO}_2^{\text{atm}}$  is measured, the soft-tissue-pump regenerated DIC inventory can be estimated from measurements of apparent oxygen utilization (AOU, Broecker et al., 1985; Ito & Follows, 2005), and the solubility and piston-velocities can be derived from the observed temperature and wind fields (as they were in this study). This leaves only the global-mean sequestration time  $\langle \Gamma_{\text{soft}} \rangle$  to be determined from a model. We did not find the global-mean  $\langle \Gamma_{\text{soft}} \rangle$  to be sensitive to  $K$ -weighting or to whether injection or regeneration tagging was employed. For the current state of the ocean,  $\langle \Gamma_{\text{soft}} \rangle$  is also likely not very sensitive to model details and our estimates of  $\langle \Gamma_{\text{soft}} \rangle$  could be used for an otherwise observation-based estimate of  $\langle \bar{m}_{\text{soft}} \rangle_{\Gamma K}$ . The distributions of isotopes that fractionate on

photosynthesis and/or respiration may provide additional constraints to be explored in future work. In the context of more detailed mechanistic models, the passage-counting-based diagnostics considered here will likely provide valuable insight into the workings of the ocean's biological pump.

## 7. Conclusions

We have presented the number of carbon passages per DIC molecule through the soft-tissue or carbonate pumps as a new metric of the efficiency of these pumps, and have introduced the injection-tagged sequestration time to establish a quantitative link between the mean number of future pump passages at the surface and atmospheric  $p\text{CO}_2$ . We have illustrated these new concepts using a data-constrained optimized model of the coupled carbon and phosphorus cycles embedded in a data-assimilated ocean circulation inverse model. Our key findings are:

For the unperturbed observationally constrained state of the biological pump, on average a fraction  $F_{\text{soft}} = 40\%–47\%$  of the DIC in a given water parcel makes at least one lifetime passage through the soft-tissue pump and a fraction  $F_{\text{carb}} \sim 4\%$  makes at least one lifetime passage through the carbonate pump. Including the fraction making zero passages, the global mean number of lifetime soft-pump passages per DIC molecule is  $\bar{N}_{\text{soft}} = 0.57–0.73$ . Correspondingly, 30%–37% of the carbon that passes through the soft-tissue pump makes more than one passage, while only about 2% of the carbon that passes through the carbonate pump makes more than one passage. As biological uptake is strengthened to completely deplete surface  $\text{PO}_4$ ,  $F_{\text{soft}}$  increases by a factor of roughly 1.6, while  $\bar{N}_{\text{soft}}$  increases by a factor of  $\sim 2.4$ . For the carbonate pump, both  $F_{\text{carb}}$  and  $\bar{N}_{\text{carb}}$  increase by a factor of  $\sim 1.8$ .

The number of future passages through the soft-tissue and carbonate pumps at the surface,  $\bar{m}_{\text{soft}}(\mathbf{r}_s)$  and  $\bar{m}_{\text{carb}}(\mathbf{r}_s)$ , are local metrics of the pump efficiencies that measure the globally integrated rate of aphotic DIC regeneration resulting from a unit atmospheric  $\text{CO}_2$  injection rate at point  $\mathbf{r}_s$ . For the unperturbed base state, the spatial pattern of  $\bar{m}_{\text{soft}}(\mathbf{r}_s)$  has only order 10% spatial variations from its global mean of 0.25–0.32 future passages per DIC molecule. When production is perturbed and shifted to high latitudes to drive surface nutrients to zero,  $\bar{m}_{\text{soft}}(\mathbf{r}_s)$  becomes poleward intensified and roughly doubles with a global mean of 0.49–0.68.

We have introduced the injection-tagged mean sequestration time formed by the ratio of the regenerated DIC inventory per unit  $\text{CO}_2$  injection area to the corresponding globally integrated aphotic regenerate rate. For the soft-tissue pump, the injection-tagged sequestration time is order 100 years, with a pattern that is largest at high latitudes where injection can deliver DIC to uptake and regeneration in deep-water formation regions. For the carbonate pump, the injection-tagged sequestration time is largest in the central and subarctic Pacific where deep  $\text{CaCO}_3$  dissolution accesses the ocean's oldest waters. Optimized states with a twofold shorter prescribed respiration timescale have roughly 25% shorter soft-pump sequestration times and correspondingly a roughly 30% higher mean number of soft-pump passages.

We recast the approximate expression of Kwon et al. (2011), relating the fractional change in  $p\text{CO}_2^{\text{atm}}$  to changes in the regenerated carbon inventories, in terms of the fractional changes in the surface-mean number of future pump passages and the corresponding injection-tagged sequestration times. For our model, natural atmospheric  $p\text{CO}_2$  (anthropogenic component removed) ranges from  $493 \pm 1$  ppmv for an abiotic ocean to  $207 \pm 1$  ppmv at complete surface nutrient depletion. Our approximate theoretical expression allows us to reconstruct the perturbed values of  $p\text{CO}_2^{\text{atm}}$  from the fractional changes in the mean number of future pump passages and in the mean sequestration times to within 5% for  $p\text{CO}_2^{\text{atm}} > 214$  ppmv. Our analysis suggests that the sensitivity of  $p\text{CO}_2^{\text{atm}}$  to changes in the oceanic carbon cycle is dominated by changes in the surface-averaged values of the mean number of future passages  $\bar{m}_{\text{soft}}$  through the soft-tissue pump.

By tracking carbon throughout its lifetime in the ocean and keeping count of the number of passages through the soft-tissue and carbonate pumps, the conceptually new diagnostics presented here provide more mechanistic, locally defined metrics of pump efficiency than the global fractions of regenerated DIC

or the fraction of regenerated  $\text{PO}_4$ . Our analysis provides a quantitative framework for clarifying the roles of the mean number of lifetime pump passages following injection from the atmosphere and of the mean time that the resulting DIC spends in the aphotic zone in controlling atmospheric  $\text{pCO}_2$ . As models of the carbon cycle embedded in circulation models via transport matrices become more common, the diagnostics of carbon cycling developed here can be adopted relatively easily to different biogeochemical models and circulations to provide insight into the mechanistic control of the biological pump on atmospheric  $\text{pCO}_2$  levels in current, past, and future climates.

## Appendix A: Objective Function and Optimized Parameter Values

The objective function,  $E$ , is constructed from the mismatches  $\delta\chi = \chi_{\text{mod}} - \chi_{\text{obs}}$ . Organizing these fields into column vectors,  $E$  is given by

$$E = \frac{\delta_{\text{DIC}}^T \hat{\mathbf{w}} \delta_{\text{DIC}}}{\sigma_{\text{DIC}}^2} + \frac{\delta_{\text{PO}_4}^T \hat{\mathbf{w}} \delta_{\text{PO}_4}}{\sigma_{\text{PO}_4}^2} + \frac{\delta_{\text{TA}}^T \hat{\mathbf{w}} \delta_{\text{TA}}}{\sigma_{\text{TA}}^2}, \quad (\text{A1})$$

where  $\sigma_\chi^2 = (\chi - \bar{\chi})^T \hat{\mathbf{w}} (\chi - \bar{\chi})$  is the spatial variance of field  $\chi$  (overbar denotes the volume-weighted global mean), and  $\hat{\mathbf{w}} = \text{diag}(\hat{w})$ , where  $\hat{w}$  is the vector of grid-box volumes divided by the global ocean volume (fractional grid-box volumes).  $E$  is minimized numerically to determine the optimized parameter values collected in Table A1, which also shows the corresponding RMS values for the mismatch between model and observations. The uncertainties reported in Table A1 simply represent the half-range difference between using the VGPM and CbPM estimates for NPP. A more complete, though still ad-hoc measure of uncertainty is the difference between the case with optimized respiration timescale  $\kappa_{\text{dop}}^{-1}$  and the case where  $\kappa_{\text{dop}}^{-1}$  is fixed at 1.2 years. Uncertainties reported in the main text are the half-range across the four states (two NPP cases and two respiration timescales), which is dominated by the difference in  $\kappa_{\text{dop}}$ .

**Table A1**  
Numerical Values of Key Biogeochemical Parameters (\* Not Optimized) and Fit Metrics

Parameter	Description	Value	Value	Units
		( $\kappa_{\text{doc}}$ optimized)	( $\kappa_{\text{doc}}$ prescribed)	
$\alpha$	Production amplitude	$48.0 \pm 0.8$	$79.5 \pm 0.7$	$\mu\text{M C/year}$
$\beta$	Production NPP exponent	$0.300 \pm 0.001$	$0.26 \pm 0.01$	–
$\sigma$	Fraction of DOM production	$0.518 \pm 0.001$	$0.675 \pm 0.008$	–
$R$	PIC/POC rain ratio	$6.95 \pm 0.05$	$6.93 \pm 0.03$	%
$b$	Martin exponent	$0.975 \pm 0.001$	$0.975 \pm 0.001$	–
$L_{\text{PIC}}$	PIC remin. length	$4.54 \pm 0.04$	$4.39 \pm 0.01$	km
$\kappa_{\text{dop}}^{-1} = \kappa_{\text{doc}}^{-1}$	Respiration timescale	$2.5 \pm 0.1$	1.2*	years
$k_{\text{pop}}^{-1} = k_{\text{poc}}^{-1} = k_{\text{pic}}^{-1}$	Particle dissolution timescales	1*	1*	days
$m_{\text{PC}}$	$d(\text{P:C})/d[\text{PO}_4]$	$3.3 \pm 0.1$	$2.9 \pm 0.1$	$(\mu\text{M PO}_4)^{-1}$
$b_{\text{PC}}$	P:C intercept at $[\text{PO}_4] = 0$	$7.12 \pm 0.06$	$7.46 \pm 0.08$	–
–	Export C:P stoichiometry	$108.9 \pm 0.1$	$107.8 \pm 0.2$	mol C/mol P
–	RMS mismatch of DIC	$19.066 \pm 0.003$	$19.29 \pm 0.04$	$\mu\text{M}$
–	RMS mismatch of $\text{PO}_4$	$0.1531 \pm 0.0003$	$0.1552 \pm 0.0002$	$\mu\text{M}$
–	RMS mismatch of TA	$13.88 \pm 0.02$	$13.76 \pm 0.02$	$\mu\text{M}$
–	(Total mismatch variance, $E/3$ )	$6.338 \pm 0.004$	$6.370 \pm 0.008$	%

## Appendix B: Carbon Utilization and Regenerated DIC

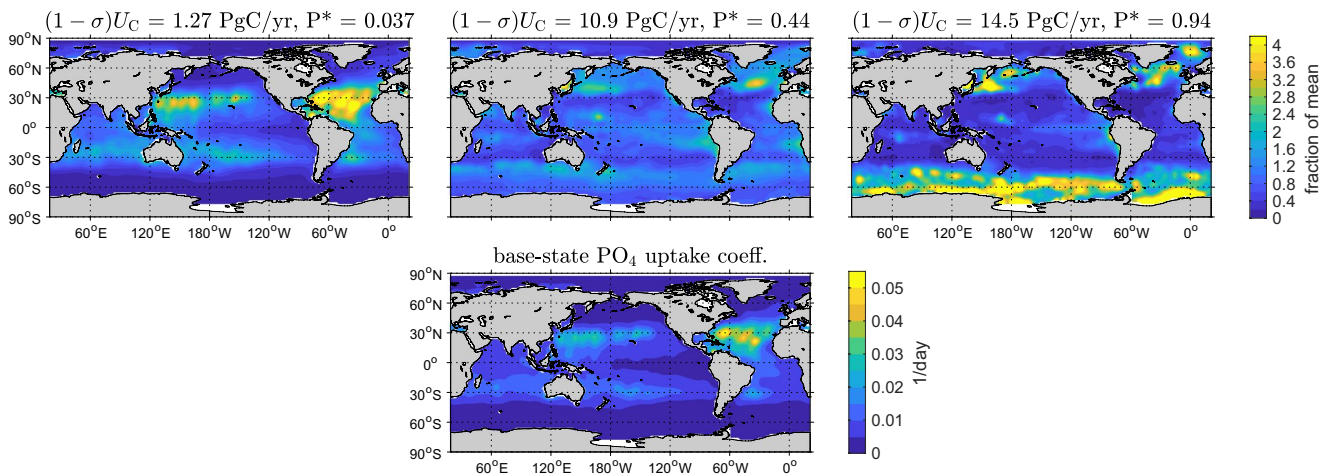
The top row of plots of Figure B1 shows the pattern of the vertically integrated DIC uptake  $U_C$  for three selected states of the biological pump: throttled ( $P^* = 0.037$ ), base-state ( $P^* = 0.44$ ), and strong ( $P^* = 0.94$ ). Note that even for the strong case, the global POC production rate [global volume integral of  $(1 - \sigma)U_C$ ] increases only by some 30% from the unperturbed base state as nutrient depletion limits further organic-matter production and POC export.  $U_C$  is parameterized in terms of an NPP-based pattern of inverse  $PO_4$  uptake timescales  $\mathcal{L}$  shown in the bottom plot of Figure B1. As the strength of the pump is turned down, the  $PO_4$  concentration homogenizes and the pattern of  $U_C$  becomes the pattern of  $R_{C,P}$ . As the strength of the pump is cranked up,  $PO_4$  becomes increasingly trapped at high latitudes and the maxima of DIC (and nutrient) utilization move poleward.

Figure B2 shows the basin zonal means of (a) the concentration of DIC regenerated by the respiration of DOC, and (b) DIC regenerated by the dissolution of biogenic calcium carbonate (PIC).

## Appendix C: Regeneration-Tagged Sequestration Times and Injection-Tagged Carbonate-Pump Sequestration Times

Figures C1a and C1b show the regeneration-tagged sequestration times of the soft-tissue and carbonate pumps. Regeneration tagging means that the sequestration time at surface point  $\mathbf{r}_s$  is associated with a unit DIC regeneration rate beneath  $\mathbf{r}_s$ . As explained in the main text, the regeneration-tagged sequestration time changes very little with the uptake pattern; it is plotted here for the unperturbed base state.

Figure C1c shows the injection-tagged sequestration time for the carbonate pump. The injection-tagged sequestration time at surface point  $\mathbf{r}_s$  is associated with a unit DIC regeneration rate that traces back to where the carbon was injected from the atmosphere at point  $\mathbf{r}_s$ . We calculate the resulting regeneration field, which is now geographically distributed by transport from injection to uptake, and the mean time for the resulting regenerated DIC distribution to return to the euphotic zone. Because the regeneration field accessed from a given injection point does depend on the pattern of biological production, the injection-tagged sequestration time depends more strongly on the state of the biological pump, parameterized here by  $P^*$ .



**Figure B1.** Top row of plots: The POC production rate  $(1 - \sigma)U_C$  vertically integrated over the euphotic zone and normalized by its global mean. The value of the global integral is given in the plot titles. Bottom plot: The phosphate uptake rate-coefficients  $\mathcal{L}$  that determine DIC uptake as  $U_C = R_{C,P}\mathcal{L}[PO_4]_{\text{mod}}$ .

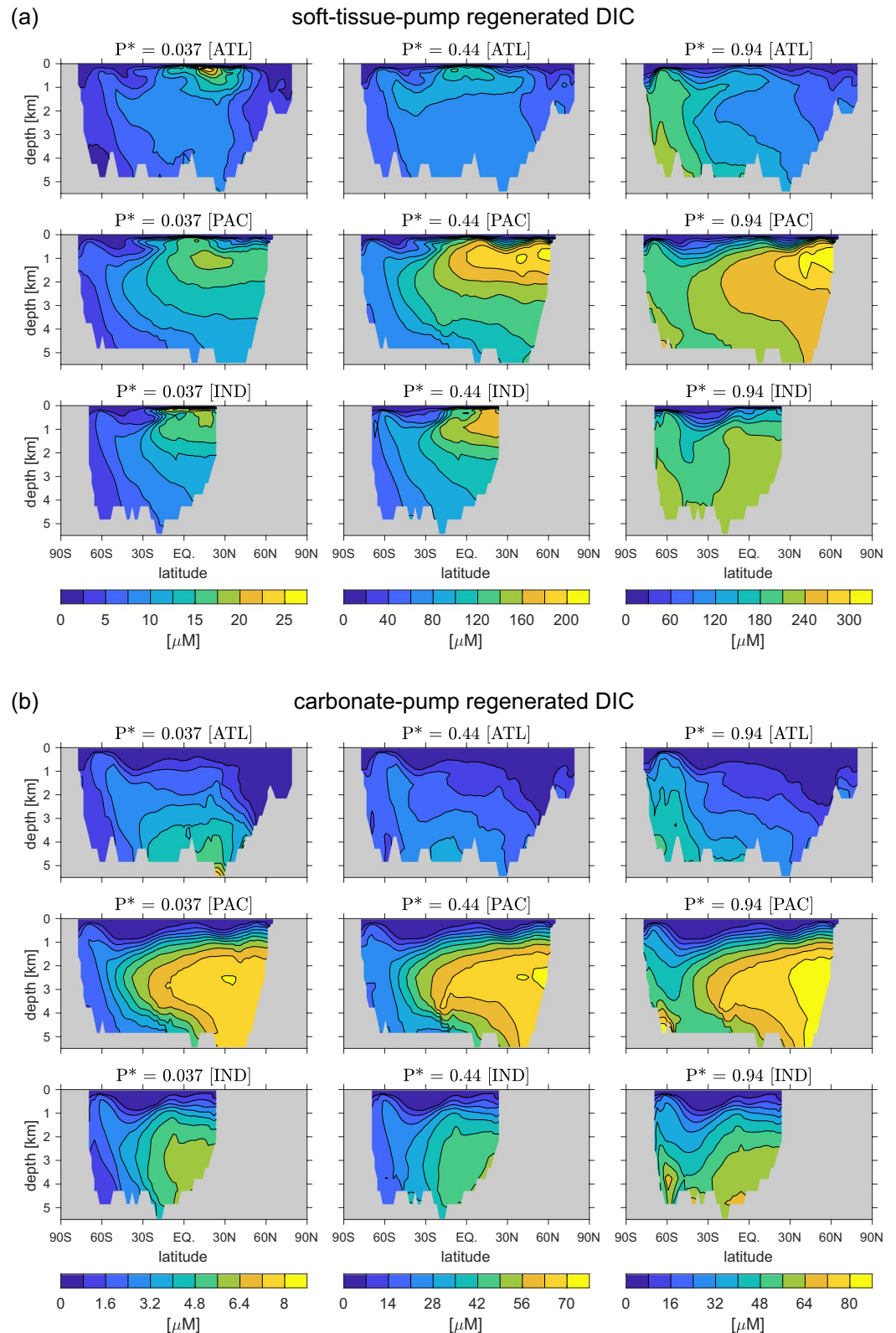


**Figure B2.** (a) The concentrations of soft-tissue-pump regenerated DIC (respired organic carbon) zonally averaged for each basin (top ATLantic, middle PACific, bottom INDian ocean) and for three selected states of the biological pump. The middle column of plots shows the base state ( $P^* = 0.44$ ), the left column of plots shows the strongly throttled carbon pump ( $P^* = 0.037$ ), and right column shows the strongly stimulated carbon pump ( $P^* = 0.94$ ). (b) As (a) for the carbonate-pump regenerated DIC (dissolved  $\text{CaCO}_3$ ).

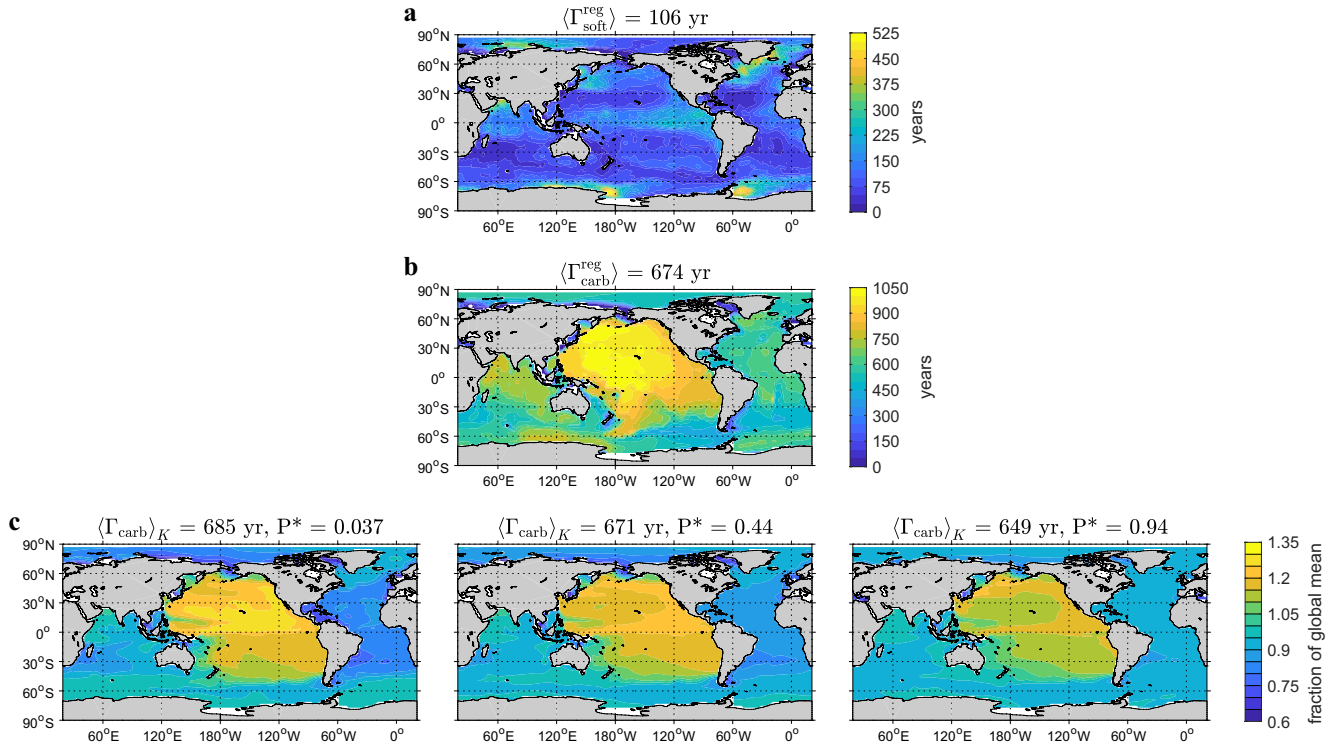


**Figure C1.** The regeneration-tagged mean sequestration times of (a) the soft-tissue pump and (b) the calcium carbonate pump. (Regeneration-tagged means that the value of the sequestration time is plotted where the regeneration occurred.) (c) The injection-tagged mean sequestration times of the calcium carbonate pump plotted as in Figure 3.

## Appendix D: Changes in $p\text{CO}_2^{\text{atm}}$ and the Regenerated DIC Inventories

The effective  $p\text{CO}_2^{\text{ocn}}$  in seawater can be considered to be a function of DIC and TA. Small changes  $\delta\text{DIC}$  and  $\delta\text{TA}$  thus induce changes  $\delta p\text{CO}_2^{\text{ocn}} = (\partial p\text{CO}_2^{\text{ocn}} / \partial \text{DIC})\delta\text{DIC} + (\partial p\text{CO}_2^{\text{ocn}} / \partial \text{TA})\delta\text{TA}$ . If we neglect changes in disequilibrium so that at the surface  $\delta p\text{CO}_2^{\text{ocn}} / p\text{CO}_2^{\text{ocn}} = \delta p\text{CO}_2^{\text{atm}} / p\text{CO}_2^{\text{atm}}$  and replace DIC and TA by their surface averages  $\langle \text{DIC} \rangle$  and  $\langle \text{TA} \rangle$ , the fractional change in  $p\text{CO}_2^{\text{atm}}$  can be written as

$$\frac{\delta p\text{CO}_2^{\text{atm}}}{p\text{CO}_2^{\text{atm}}} = R_C \frac{\delta \langle \text{DIC} \rangle}{\langle \text{DIC} \rangle} + R_A \frac{\delta \langle \text{TA} \rangle}{\langle \text{TA} \rangle}, \quad (\text{D1})$$

where  $R_C$  and  $R_A$  are suitable average values of the Revelle buffer factor  $\partial \log(p\text{CO}_2^{\text{ocn}}) / \partial \log(\text{DIC})$  and alkalinity factor  $\partial \log(p\text{CO}_2^{\text{ocn}}) / \partial \log(\text{TA})$ , respectively. If we further approximate the surface-mean DIC and TA concentrations by the global volume-averaged preformed means,  $C^{\text{pre}}$  and  $A^{\text{pre}}$ , we can express the right-hand-side of Equation D1 in term of the changes in the global-mean regenerated DIC concentrations,  $C_{\text{soft}}$  and  $C_{\text{carb}}$ . Assuming conservation of carbon in the atmosphere-ocean system (no change in terrestrial reservoirs), which has a negligible atmospheric contribution, and neglecting the POC, PIC, and semilabile DOC pools compared to DIC, we have  $\delta C^{\text{pre}} = -\delta C_{\text{soft}}^{\text{reg}} - \delta C_{\text{carb}}^{\text{reg}}$ . Similarly assuming global conservation of TA, we have  $\delta A^{\text{pre}} = -2\delta C_{\text{carb}}^{\text{reg}} + R_{\text{N:C}}\delta C_{\text{soft}}^{\text{reg}}$ . Substituting into Equation D1 obtains the result of Kwon et al. (2011):

$$\frac{\delta p\text{CO}_2^{\text{atm}}}{p\text{CO}_2^{\text{atm}}} = \mathcal{R}_s \delta C_{\text{soft}}^{\text{reg}} + \mathcal{R}_c \delta C_{\text{carb}}^{\text{reg}} \quad (\text{D2})$$

where  $\mathcal{R}_s = -R_C / C^{\text{pre}} + R_{\text{N:C}}R_A / A^{\text{pre}}$  and  $\mathcal{R}_c = -R_C / C^{\text{pre}} - 2R_A / A^{\text{pre}}$ .

From Equation 20, we have for the  $p$  pump ( $p$  is soft or carb):

$$\frac{\delta C_p^{\text{reg}}}{C_p^{\text{reg}}} = \frac{\delta p\text{CO}_2^{\text{atm}}}{p\text{CO}_2^{\text{atm}}} + \frac{\delta \langle \bar{m}_p \rangle_{K\Gamma}}{\langle \bar{m}_p \rangle_{K\Gamma}} + \frac{\delta \langle \Gamma_p \rangle_K}{\langle \Gamma_p \rangle_K} \quad (\text{D3})$$

Re-arranging for  $\delta C_{\text{soft}}^{\text{reg}}$  and  $\delta C_{\text{carb}}^{\text{reg}}$ , substituting into Equation D2 and solving for  $\delta p\text{CO}_2^{\text{atm}} / p\text{CO}_2^{\text{atm}}$  gives Equation 21 of the main text, with

$$\mathcal{M}_s = \frac{\mathcal{R}_s C_{\text{soft}}^{\text{reg}}}{1 - \mathcal{R}_s C_{\text{soft}}^{\text{reg}} - \mathcal{R}_c C_{\text{carb}}^{\text{reg}}} \quad \text{and} \quad \mathcal{M}_c = \frac{\mathcal{R}_c C_{\text{carb}}^{\text{reg}}}{1 - \mathcal{R}_s C_{\text{soft}}^{\text{reg}} - \mathcal{R}_c C_{\text{carb}}^{\text{reg}}} \quad (\text{D4})$$

## Data Availability Statement

The data used for this study are available from the following archives; no new data were used. The gridded temperature, salinity, and nutrient data are available at <https://www.ncei.noaa.gov/products/world-ocean-atlas>. The DIC and TA data are available at <https://www.nodc.noaa.gov/ocads/oceans/GLODAPv2>. The NPP data used are available at <http://sites.science.oregonstate.edu/ocean.productivity>. The atmospheric pCO<sub>2</sub> data are available at <http://data.giss.nasa.gov/modelforce/ghgases> and <https://cdiac.ess-dive.lbl.gov/trends/co2/lawdome-data.html>.

## Acknowledgments

The authors acknowledge helpful conversations with Francois Primeau and Tim DeVries. This study was supported by ARC Grant DP210101650 (Mark Holzer) and by Grants IBS-R028-D1 and NRF-2016R1D1A1B04931356 (Eun Y. Kwon).

## References

- Archer, D. E., Eshel, G., Winguth, A., Broecker, W., Pierrehumbert, R., Tobis, M., & Jacob, R. (2000). Atmospheric pCO<sub>2</sub> sensitivity to the biological pump in the ocean. *Global Biogeochemical Cycles*, 14, 1219–1230. <https://doi.org/10.1029/1999GB001216>
- Bacastow, R., & Maier-Reimer, E. (1990). Ocean-circulation model of the carbon cycle. *Climate Dynamics*, 4, 95–125.
- Battaglia, G., Steinacher, M., & Joos, F. (2016). A probabilistic assessment of calcium carbonate export and dissolution in the modern ocean. *Biogeosciences*, 13, 2823–2848. <https://doi.org/10.5194/bg-13-2823-2016>
- Behrenfeld, M. J., & Falkowski, P. G. (1997). Photosynthetic rates derived from satellite-based chlorophyll concentration. *Limnology & Oceanography*, 42, 1–20.
- Broecker, W. S., Takahashi, T., & Takahashi, T. (1985). Sources and flow patterns of deep-ocean waters as deduced from potential temperature, salinity, and initial phosphate concentration. *Journal of Geophysical Research*, 90(C4), 6925–6939.
- Bronk, D. A., See, J. H., Bradley, P., & Killber, L. (2007). DON as a source of bioavailable nitrogen for phytoplankton. *Biogeosciences*, 4, 283–296.
- Buesseler, K. O., Boyd, P. W., Black, E. E., & Siegel, D. A. (2020). Metrics that matter for assessing the ocean biological carbon pump. *Proceedings of the National Academy of Sciences of the United States of America*, 117, 9679–9687. <https://doi.org/10.1073/pnas.1918114117>
- Cameron, D. R., Lenton, T. M., Ridgwell, A. J., Shepherd, R. J. G., Marsh, & Yool, A. (2005). A factorial analysis of the marine carbon cycle and ocean circulation controls on atmospheric CO<sub>2</sub>. *Global Biogeochemical Cycles*, 19, GB4027. <https://doi.org/10.1029/2005GB002489>
- Chamberlain, M. A., Matear, R. J., Holzer, M., Bi, D., & Marsland, S. J. (2019). Transport matrices from standard ocean-model output and quantifying circulation response to climate change. *Ocean Modelling*, 135, 1–13. <https://doi.org/10.1016/j.ocemod.2019.01.005>
- DeVries, T. (2014). The oceanic anthropogenic CO<sub>2</sub> sink: Storage, air-sea fluxes, and transports over the industrial era. *Global Biogeochemical Cycles*, 28(7), 631–647.
- DeVries, T., & Holzer, M. (2019). Radiocarbon and helium isotope constraints on deep-ocean ventilation and mantle-<sup>3</sup>He sources. *Journal of Geophysical Research: Oceans*, 124, 3036–3057. <https://doi.org/10.1002/2018JC014716>
- DeVries, T., Primeau, F., & Deutsch, C. (2012). The sequestration efficiency of the biological pump. *Geophysical Research Letters*, 39, L13601. <https://doi.org/10.1029/2012GL051963>
- DeVries, T., & Weber, T. (2017). The export and fate of organic matter in the ocean: New constraints from combining satellite and oceanographic tracer observations. *Global Biogeochemical Cycles*, 31, 535–555. <https://doi.org/10.1002/2016GB005551>
- Dlugokencky, E. J., Mund, J., Crotwell, A., Crotwell, M., & Thoning, K. (2021). *Atmospheric carbon dioxide dry air mole fractions from the NOAA GML carbon cycle cooperative global air sampling network, 1968-2019, 2021-02*. National Oceanic and Atmospheric Administration, Global Monitoring Laboratory. <https://doi.org/10.15138/wkgj-f215>
- Ducklow, H. W., Steinberg, D. K., & Buesseler, K. O. (2001). Upper ocean carbon export and the biological pump. *Oceanography*, 14, 50–58. <https://doi.org/10.5670/oceanog.2001.06>
- Dugdale, R. C., & Goering, J. J. (1967). Uptake of new and regenerated forms of nitrogen in primary productivity. *Limnology & Oceanography*, 12, 196–206.
- Eppley, R., & Peterson, B. (1979). Particulate organic matter flux and planktonic new production in the deep ocean. *Nature*, 282, 677–680. <https://doi.org/10.1038/282677a0>
- Etheridge, D. M., Barnola, J. M., Morgan, V. I., Steele, L. P., Langenfelds, R. L., Francey, R. J., & Martinez, M. (1998). Historical CO<sub>2</sub> Records from the Law Dome DE08, DE08-2, and DSS Ice Cores (1006 A.D.-1978 A.D.). <https://doi.org/10.3334/CDIAC/ATG.011>
- Etheridge, D. M., Steele, L. P., Langenfelds, R. L., Francey, R. J., Barnola, J., & Morgan, V. I. (1996). Natural and anthropogenic changes in atmospheric CO<sub>2</sub> over the last 1000 years from air in Antarctic ice and firn. *Journal of Geophysical Research*, 101, 4115–4128. <https://doi.org/10.1029/95JD03410>
- Galbraith, E. D., & Martiny, A. C. (2015). A simple nutrient-dependence mechanism for predicting the stoichiometry of marine ecosystems. *Proceedings of the National Academy of Sciences of the United States of America*, 112, 8199–8204. <https://doi.org/10.1073/pnas.1423917112>
- Garcia, H. E., Locarnini, R. A., Boyer, T. P., & Antonov, J. I. (2010). In S. Levitus, Ed., *World Ocean Atlas 2009, volume 4: Nutrients (phosphate, nitrate, silicate)*. U.S. Government Printing Office.

- Gnanadesikan, A., Slater, R., Gruber, N., & Sarmiento, J. (2002). Oceanic vertical exchange and new production: A comparison between models and observations. *Deep Sea Research Part II: Topical Studies in Oceanography*, *49*, 363–401.
- Hain, M. P., Sigman, D. M., & Haug, G. H. (2014). The biological pump in the past. In H. D. Holland, & K. K. Turekian, (Eds.), *Treatise on geochemistry* (2nd ed., pp. 485–517). Elsevier Inc. <https://doi.org/10.1016/B978-0-08-095975-7.00618-5>
- Hansell, D. A., Carlson, C. A., & Schlitzer, R. (2012). Net removal of major marine dissolved organic carbon fractions in the subsurface ocean. *Global Biogeochemical Cycles*, *26*, GB1016. <https://doi.org/10.1029/2011GB004069>
- Holzer, M., Chamberlain, M. A., & Matear, R. J. (2020). Climate-driven changes in the ocean's ventilation pathways and timescales diagnosed from transport matrices. *Journal of Geophysical Research: Oceans*, *125*(4), e2020JC016414. <https://doi.org/10.1029/2020JC016414>
- Holzer, M., Primeau, F. W., DeVries, T., & Matear, R. (2014). The Southern Ocean silicon trap: Data-constrained estimates of regenerated silicic acid, trapping efficiencies, and global transport paths. *Journal of Geophysical Research: Oceans*, *119*(1), 313–331. <https://doi.org/10.1002/2013JC009356>
- Honda, M. C. (2020). Effective vertical transport of particulate organic carbon in the Western North Pacific Subarctic Region. *Frontiers of Earth Science*, *8*, 366. <https://doi.org/10.3389/feart.2020.00366>
- Ito, T., & Follows, M. J. (2005). Preformed phosphate, soft tissue pump and atmospheric CO<sub>2</sub>. *Journal of Marine Research*, *63*, 813–839.
- John, S., Liang, H., Weber, T., DeVries, T., Primeau, F., Moore, K., et al. (2020). AWESOME OCIM: A simple, flexible, and powerful tool for modeling elemental cycling in the oceans. *Chemical Geology*, *533*. <https://doi.org/10.1016/j.chemgeo.2019.119403>
- Kalnay, E., Kanamitsu, M., Kistler, R., Collins, W., Deaven, D., Gandin, L., et al. (1996). The NMC/NCAR 40-year reanalysis project. *Bulletin of the American Meteorological Society*, *77*, 437–471.
- Keeling, C. D., Piper, S. C., Bacastow, R. B., Wahlen, M., Whorf, T. P., Heimann, M., & Meijer, H. A. (2005). Atmospheric CO<sub>2</sub> and 13CO<sub>2</sub> exchange with the terrestrial biosphere and oceans from 1978 to 2000: Observations and carbon cycle implications. In J. Ehleringer, T. E. Cerling, & M. D. Dearing, (Eds.), *A history of atmospheric CO<sub>2</sub> and its effects on plants, animals, and ecosystems* (pp. 83–113). Springer Verlag.
- Kvale, K. F., Khatiwala, S., Dietze, H., Kriest, I., & Oschlies, A. (2017). Evaluation of the transport matrix method for simulation of ocean biogeochemical tracers. *Geoscientific Model Development*, *10*, 2425–2445. <https://doi.org/10.5194/gmd-10-2425-2017>
- Kwon, E. Y., & Primeau, F. (2008). Optimization and sensitivity of a global biogeochemistry ocean model using combined in-situ DIC, alkalinity and phosphate data. *Journal of Geophysical Research*, *113*. C08011. <https://doi.org/10.1029/2007JC004520>
- Kwon, E. Y., Primeau, F. W., & Sarmiento, J. L. (2009). The impact of remineralization depth on the air-sea carbon balance. *Nature Geoscience*, *2*, 630–635. <https://doi.org/10.1038/ngeo612>
- Kwon, E. Y., Sarmiento, J. L., Toggweiler, J. R., & DeVries, T. (2011). The control of atmospheric pCO<sub>2</sub> by ocean ventilation change: The effect of the oceanic storage of biogenic carbon. *Global Biogeochemical Cycles*, *25*, GB3026. <https://doi.org/10.1029/2011GB004059>
- Letscher, R. T., & Moore, J. K. (2015). Preferential remineralization of dissolved organic phosphorus and non-Redfield DOM dynamics in the global ocean: Impacts on marine productivity, nitrogen fixation, and carbon export. *Global Biogeochemical Cycles*, *29*, 325–340. <https://doi.org/10.1002/2014GB004904>
- Marsay, C. M., Sanders, R. J., Henson, S. A., Pabortsava, K., & Lampitt, E. P. A. R. S. (2015). Attenuation of sinking particulate organic carbon flux through the mesopelagic ocean. *Proceedings of the National Academy of Sciences of the United States of America*, *112*, 1089–1094. <https://doi.org/10.1073/pnas.1415311112>
- McKinley, G. A., Fay, A. R., Lovenduski, N. S., & Pilcher, D. J. (2017). Natural variability and anthropogenic trends in the ocean carbon sink. *Annual Review of Marine Science*, *9*, 125–150. <https://doi.org/10.1146/annurev-marine-010816-060529>
- Murnane, R. J., Sarmiento, J. L., & Le Quéré, C. (1999). Spatial distribution of air-sea CO<sub>2</sub> fluxes and the interhemispheric transport of carbon by the oceans. *Global Biogeochemical Cycles*, *13*, 287–305. <https://doi.org/10.1029/1998GB900009>
- Najjar, R. G., Sarmiento, J. L., & Toggweiler, J. R. (1992). Downward transport and fate of organic matter in the ocean: Simulations with a general circulation model. *Global Biogeochemical Cycles*, *6*, 45–76.
- Olsen, A., Key, R. M., van Heuven, S., Lauvset, S. K., Velo, A., Lin, X., et al. (2016). The Global Ocean Data Analysis Project version 2 (GLODAPv2) – An internally consistent data product for the world ocean. *Earth System Science Data*, *8*, 297–323. <https://doi.org/10.5194/essd-8-297-2016>
- Pasquier, B., & Holzer, M. (2016). The plumbing of the global biological pump: Efficiency control through leaks, pathways, and time scales. *Journal of Geophysical Research*, *121*(8), 6367–6388. <https://doi.org/10.1002/2016JC011821>
- Pasquier, B., & Holzer, M. (2018). The number of past and future regenerations of iron in the ocean and its intrinsic fertilization efficiency. *Biogeosciences*, *15*, 7177–7203. <https://doi.org/10.5194/bg-15-7177-2018>
- Primeau, F. W., Holzer, M., & DeVries, T. (2013). Southern Ocean nutrient trapping and the efficiency of the biological pump. *Journal of Geophysical Research*, *118*, 2547–2564. <https://doi.org/10.1002/jgrc.20181>
- Roshan, S., & DeVries, T. (2017). Efficient dissolved organic carbon production and export in the oligotrophic ocean. *Nature Communications*, *8*, 2036. <https://doi.org/10.1038/s41467-017-02227-3>
- Sarmiento, J. L., & Gruber, N. (2006). *Ocean biogeochemical dynamics*. Princeton University Press.
- Sarmiento, J. L., & Toggweiler, J. R. (1984). A new model for the role of oceans in determining atmospheric pCO<sub>2</sub>. *Nature*, *308*, 621–624
- Sigman, D., & Boyle, E. A. (2000). Glacial/interglacial variations in atmospheric carbon dioxide. *Nature*, *407*, 859–869.
- Teng, Y.-C., Primeau, F. W., Moore, J. K., Lomas, M. W., & Martiny, A. C. (2014). Global-scale variations of the ratios of carbon to phosphorus in exported marine organic matter. *Nature*, *7*, 895–898. <https://doi.org/10.1038/NGEO2303>
- Thoning, K., Croftwell, A., & Mund, J. (2021). *Atmospheric carbon dioxide dry air mole fractions from continuous measurements at Mauna Loa, Hawaii, Barrow, Alaska American Samoa and South Pole, 1973-2019, 2021-02*. National Oceanic and Atmospheric Administration, Global Monitoring Laboratory. <https://doi.org/10.15138/yaf1-bk21>
- van Heuven, S., Pierrot, D., Rae, J. W. B., Lewis, E., & Wallace, D. W. R. (2011). *MATLAB program developed for CO<sub>2</sub> system calculations, ORNL/CDIAC-105b, Carbon Dioxide Information Analysis Center*. Oak Ridge National Laboratory, US DOE.
- Volk, T., & Hoffert, M. I. (1985). Ocean carbon pumps: Analysis of relative strengths and efficiencies in ocean-driven atmospheric CO<sub>2</sub> changes. In E. T. Sundquist, & W. S. Broecker, (Eds.), *The carbon cycle and atmospheric CO<sub>2</sub>: Natural variations Archean to present*, Geophysical Monograph Series (Vol. 32, pp. 99–110). American Geophysical Union.
- Wanninkhof, R. (1992). Relationship between wind speed and gas exchange over the ocean. *Journal of Geophysical Research*, *97*, 7373–7382.
- Wanninkhof, R., Park, G.-H., Takahashi, T., Sweeney, C., Feely, R., Nojiri, Y., et al. (2013). Global ocean carbon uptake: Magnitude, variability and trends. *Biogeosciences*, *10*, 1983–2000. <https://doi.org/10.5194/bg-10-1983-2013>
- Weber, T., Crama, J. A., Leung, S. W., DeVries, T., & Deutsch, C. (2016). Deep ocean nutrients imply large latitudinal variation in particle transfer efficiency. *Proceedings of the National Academy of Sciences of the United States of America*, *113*, 8606–8611. <https://doi.org/10.1073/pnas.1604414113>

- Weiss, R. F. (1974). Carbon dioxide in water and seawater: The solubility of a non-ideal gas. *Marine Chemistry*, 2, 203–215. [https://doi.org/10.1016/0304-4203\(74\)90015-2](https://doi.org/10.1016/0304-4203(74)90015-2)
- Westberry, T., Behrenfeld, M., Siegel, D., & Boss, E. (2008). Carbon-based primary productivity modeling with vertically resolved photoacclimation. *Global Biogeochemical Cycles*, 22, GB2024. <https://doi.org/10.1029/2007GB003078>
- Wolf-Gladrow, D. A., Zeebe, R. E., Klaas, C., Körtzinger, A., & Dickson, A. G. (2007). Total alkalinity: The explicit conservative expression and its application to biogeochemical processes. *Marine Chemistry*, 106, 287–300. <https://doi.org/10.1016/j.marchem.2007.01.006>
- Yamanaka, Y., & Tajika, E. (1996). The role of the vertical fluxes of particulate organic matter and calcite in the oceanic carbon cycle: Studies using an ocean biogeochemical general circulation model. *Global Biogeochemical Cycles*, 10, 361–382. <https://doi.org/10.1029/96GB00634>